

## Multiscale Modelling of Cardiac Perfusion

Jack Lee, Andrew Cookson, Radomir Chabiniok, Simone Rivolo, Eoin Hyde, Matthew Sinclair, Christian Michler, Taha Sochi and Nicolas Smith

**Abstract** To elucidate the mechanisms governing coronary blood flow in health and disease requires an understanding of the structure–function relationship of the coronary system, which exhibits distinct characteristics over multiple scales. Given the complexities arising from the multiscale and distributed nature of the coronary system and myocardial mechanical coupling, computational modelling provides an indispensable tool for advancing our understanding. In this work, we describe our strategy for an integrative whole-organ perfusion model, and illustrate a series of examples which apply the framework within both basic science and clinical translation settings. In particular, the one-dimensional reduced approach common in vascular modelling is combined with a new poromechanical formulation of the myocardium that is capable of reproducing the full contractile cycle, to enable simulation of the dynamic coronary and myocardial blood flow. In addition, a methodology for estimating continuum porous medium parameters from discrete network geometry is presented. The benefit of this framework is first demonstrated via an application to coronary wave intensity analysis, a technique developed to study time-dependent aspects of pulse waves invasively measured in the vessels. It is shown that, given experimentally-acquired boundary conditions the 1D model is capable of reproducing a wave behaviour broadly consistent with that observed *in vivo*, however, its utility is limited to a phenomenological level. The integrated 1D-poromechanical model on the other hand enables a mechanistic investigation of wave generation thus allowing the influence of contractile function and distal hemodynamic states on coronary flow to be described. In addition, when coupled with the advection-

---

J. Lee · A. Cookson · R. Chabiniok · S. Rivolo · E. Hyde · M. Sinclair · C. Michler · T. Sochi  
Department of Biomedical Engineering, Division of Imaging Sciences and Biomedical Engineering, King's College London, King's Health Partners, St. Thomas' Hospital, London, SE1 7EH, United Kingdom  
e-mail: jack.lee@kcl.ac.uk

N. Smith (✉)  
Faculty of Engineering, The University of Auckland, Auckland, New Zealand  
e-mail: np.smith@auckland.ac.nz

diffusion-reaction equation, the integrated model can be used to study the transport of tracers through the vascular network, thus allowing the dependence of noninvasive imaging signal intensities on the diffusive properties of the contrast agent to be quantified. A systematic investigation of the commonly used clinical indices and whole-organ modelling results are illustrated. Taken together, the proposed model provides a comprehensive framework with which to apply quantitative analysis in whole organ coronary artery disease diagnosis using noninvasive perfusion imaging modalities. The added value of the model in clinical practice lies in its ability to combine comprehensive patient-specific information into therapy. In this regard, we close the chapter with a discussion on potential model-aided strategies of disease management.

### 3.1 Introduction

To elucidate the mechanisms governing coronary blood flow in health and disease requires an understanding of the relationship between the structure of the coronary vasculature and its function, which exhibits distinct characteristics over multiple scales. The coronary vessels feature diameters which span over three orders of magnitude from  $\mu\text{m}$  to mm scales, and are organised in a morphometrically asymmetric branching network of vessels. A common classification of vessels derives from both structural and functional considerations, attributing major conducting, resistance, exchange and capacitance functions to the epicardial arteries, arterioles, capillaries and veins respectively. The unique mechanical environment of continual contractile cycles within which the coronary system operates, leads to a substantial fluid-structure interaction within each vessel and results in the phasic and asynchronous flow patterns observed over the vascular hierarchy. Integrated over the whole network, these interactions indirectly couple coronary blood flow to many important factors governing cardiac function, including contractility, venous return and systemic afterload.

Given the complexities arising from the multiscale and distributed nature of the coronary system and myocardial mechanical coupling, computational modelling provides an indispensable tool for advancing our understanding of cardiac function. Specifically, this approach provides the potential for quantitative and integrative insights that are currently inaccessible to experimental modes of investigation. Such a framework can be used to gain mechanistic insights into the physiological determinants of flow, aid in the design and optimisation of medical technology, and be directly applied in the clinics for diagnosis and treatment planning. The coupled fluid-structure model of coronary flow outlined in this chapter aims to bring together the principal components of the system to establish an integrated framework for investigating, and later, predicting cardiac perfusion on an individual-specific basis. Whilst the characterisation of the autoregulatory mechanisms and remodelling remains a challenge outside the current scope, in the following sections we will provide a series of examples of how our model is being applied in the realm of basic science as well as clinical translation.

## 3.2 Background

### 3.2.1 Basic Anatomy and Perfusion Territories

The large epicardial conducting arteries of the coronary network – with three main stems being left anterior descending (LAD), left circumflex (LCx) and right coronary artery (RCA) – originate from the coronary ostia situated at the aortic sinus and give rise to many intramural vessels that are predominantly oriented in the transmural direction towards the subendocardium [91]. These vessels further branch into arterioles that provide significant resistance to flow. From the terminal arterioles stem capillaries, which are closely integrated with bundles of myocytes and serve as the principal site of gas and nutrient exchange. These vessels are then collected into venules and larger veins, which finally collect blood from the coronary circulation into the right atrium via the coronary sinus. The optimal design underlying the branching patterns of vascular segments have been the subject of morphometric measurement [55], theoretical [110] and data driven [54, 62] analyses.

Aside from this intrinsic compartmentalisation of the vascular hierarchies, the sub-networks of the coronary vasculature are spatially arranged into distinct territories occupying different regions of the myocardium [91]. Typically the LAD supplies the anterolateral myocardium and a part of the septum, the LCx, the lateral wall of the left ventricle, whereas the RCA supplies the right ventricle, a part of the septum and a part of the inferior wall. The exact extension of these perfusion regions is subject to inter-individual variations, for example the inferior and inferolateral wall of the left ventricle can be supplied by RCA (the so-called right dominant coronary circulation), or by LCx (left-dominant circulation) or by both RCA and LCx (co-dominant circulation). All these possibilities are considered as variants of anatomical norm [32] and need to be reflected in the patient-specific modelling. The flow supplies to different territories are separate at the distal level [29], unless collateral vessels exist between the regions at a lower hierarchy. In healthy humans no angiographically identifiable collaterals are found, but their development in the presence of disease has been reported [36]. The functional relevance of the human coronary collaterals is gauged via indirect methods [98] and has been under debate [40, 104]. However, the beneficial effects of the recruitable collaterals to long-term survival have been documented [65].

### 3.2.2 Distribution of Resistance and Volume

Under resting conditions and intact vasomotor tone, it is estimated that approximately two thirds of the vascular resistance resides in the microvessels [18]. In this situation the large epicardial vessels contribute very little to the overall resistance unless significant stenoses are present. However, substantial redistribution of resistance may occur during vasodilation induced by exercise, a compensation due to disease or after administering a pharmacological agent e.g. during clinical examination. These changes are predominantly caused by the vasodilation taking place in the microcirculation, made possible because at resting conditions microvessels are in a

state of spontaneous constriction. The degree of such constriction (or tone) in relation to the maximal dilation of the vessel walls determines the flow reserve which can be recruited in times of increased demand.

Although estimates vary, it is reported that the coronary volume is divided among the arterial (around 20% of coronary blood volume), capillaries (approximately 30% of coronary blood volume) and venous compartments (around 50% of blood volume), altogether occupying roughly 12–15% of the total myocardial volume [90]. An important observation is that within the timescale of a single cardiac cycle, this percentage can decrease by a factor of two [52] indicating a significant storage effect in the governance of coronary flow. This capacitance is, of course, a consequence of the compliance of individual vascular segments. Experimental estimates place most of this capacitance effect as residing within veins and venules, which exhibit the largest compartmental volume and compliance.

### ***3.2.3 Mechanical Coupling of Coronary Flow and Myocardium***

Around 80% of the anterograde arterial flow occurs in the coronary system during diastole. In contrast, the venous flow is greatest during systole and is reduced in diastole. Such phasic flow patterns are the consequence of the extravascular forces interacting with the hemodynamics of the coronary system [3, 38]. During systole, the large compressive stress developed within the myocardium is transmitted to the embedded vasculature, whereupon it acts in a manner akin to a pump, driving the movement of the fluid accumulated by the enhanced proximal flow during diastole. The direction of the flow depends on the pressure gradient within the local vascular hierarchy. That is, proximal vessels are largely under the influence of the rising perfusion pressure and thus experience a reduced, but still anterograde net flow. With lower pressures in the venous vessels on the other hand, the compressive forces act to augment the net flow during systole.

The historical development of coronary-myocardial coupling has been previously reviewed [105]. Earlier modelling concepts have regarded intramyocardial pressure (IMP) to directly reflect the left ventricular cavity pressure transmitted through the extracellular space. However, subsequent experiments have demonstrated that the flow-impeding influence of myocardial contraction is of similar magnitude even when the ventricle is empty and the heart is beating against zero afterload, thereby suggesting a much stronger role of the specific microstructural coupling between the coronary vasculature and myocyte architecture. The direct action of myofibre thickening on the adjacent vessels is thus revealed as a significant driving mechanism. Conclusive evidence has been difficult to obtain due to the experimental inaccessibility of the system, however, there is a general consensus that IMP exhibits a transmural gradient and that its magnitude can exceed that of left ventricular pressure. Accordingly, the fluid-structure coupling of the coronary flow depends strongly on the hierarchical position of the vessel under consideration and its location within the myocardium, as well as the specific manner and scale of its structural coupling with the surrounding constituents of the myocardial tissue.

### 3.2.4 Invasive Clinical Indices of Coronary Disease

Coronary disease may manifest over a spectrum of disorders spanning focal/diffuse stenoses in the large vessels to microvascular dysfunction. Although they are non-mutually exclusive conditions, historically clinical investigations were mainly focussed on the large vessel disease first, perhaps due to their accessibility.

In the 1980s when coronary angiography became widely adopted, diagnosis of coronary disease focused on the anatomical measures of stenosis. Nowadays, it is known that solely-angiographic indices are poor at characterising the consequential severity of a stenosis [31, 96]. For this reason, modern clinical assessments of coronary function chiefly aim to quantify the flow reserve i.e. the capacity of the coronary system to match the supply in times of increased demand. Invasive examinations involve catheter measurements of pressure and/or velocity waveforms in selected vessels under resting and induced hyperaemic conditions. The Coronary Flow Velocity Reserve (CFVR) is a derived index, defined as the ratio of maximal hyperaemic blood flow velocity to the resting flow velocity. Whereas in healthy individuals CFVR may reach a maximum value of around 4, in disease it can be reduced below a value of 2 [37]. Note however that it is difficult to define an unambiguous clinical threshold for CFVR, since the resting flow rate is maintained at a near-constant level across a wide range of coronary pressure (thus reflecting a wide range of vasodilatory states of the distal bed) by coronary autoregulation [12].

In order to isolate a clinical assessment to focus exclusively on the stenotic severity free from confounding distal physiologic parameters, the Relative CFVR metric has been proposed. For this index, the ratio of hyperaemic velocity during maximum vasodilation in a stenotic vessel to a normal vessel velocity is calculated. In practice, however, this measure would require *a priori* knowledge of the location of normal vessels, which may be difficult to obtain (an additional catheter inside a healthy artery poses additional risk and multi-vessel disease may exist). The Fractional Flow Reserve (FFR) [78] circumvents this problem by directly measuring the ratio of pressures distal and proximal to a stenosis in the same vessel during maximal hyperaemia. This provides a surrogate measure of the hyperaemic flow that is actually obtained in the presence of the stenosis versus maximum attainable flow, if the vessel were non-stenotic. FFR has the advantage of being intrinsically normalised between 0 and 1, but requires the realisation of minimal distal resistance using pharmacological means for an accurate and reproducible assessment.

In a subset of cases, CFVR and FFR will give contradictory diagnoses. These differences likely reflect the divergent extremes of the balance between large and small vessel diseases, and reinforce the point that a full understanding of coronary disease requires characterisation of both epicardial and myocardial resistance to flow [51].

### 3.2.5 Non-invasive Imaging Modalities

Clinically, non-invasive imaging modalities provide a low-risk and cost-effective means to stratify patient cohorts and rule out negative cases before proceeding to the more invasive and costly catheter laboratory. Broadly speaking, non-invasive

imaging may be applied in two different ways, angiographic imaging which visualises vessel lumen anatomy (using computed tomography (CT) or magnetic resonance (MR)), and perfusion imaging which focuses on characterising the delivery of blood to the myocardium. In addition, some modalities offer the means to assess localised plaque composition which is related to the risk of rupture leading to thrombosis [63, 67, 82].

While there is no clinical non-invasive angiographic imaging modality that outperforms the traditional X-ray angiography in terms of resolution, CT offers a number of advantages including the imaging of three dimensional morphology and coronary artery calcification. Modern CT scanners can offer up to 330  $\mu\text{m}$  spatial and 75 ms temporal resolution. Furthermore, large clinical studies have demonstrated that low ionisation (1–2 mSv) and contrast-free CT-derived calcium scores have a negative predictive value of 99% making it an ideal screening tool for intermediate-risk patients experiencing chest pain [74].

Patients with microvascular or multi-vessel disease, previous infarcts and other associated cardiac conditions may benefit from the diagnostic information provided by the assessment of perfusion, which is a measure of blood supplied to the cells of the organ. With these increased complexities, shifting the focus away from the large epicardial vessels to the whole myocardium can reveal a more complete picture. Perfusion imaging is often conducted with a stress-protocol, during which higher flow demand of myocardium is induced to reveal regions of unmatched supply (thus again revealing the flow reserve). Major modalities for perfusion imaging include Single Photon Emission Computed Tomography (SPECT), Positron Emission Tomography (PET) and perfusion MR Imaging. While nuclear medicine techniques have an advantage in robust absolute quantifications and have the potential to target specific metabolic consequences of tissue perfusion [8], one of the strong points of perfusion MRI lies in its significantly higher spatio-temporal resolution (1.2 mm in-plane/1 s imaging time for MRI vs 5 mm/1 min imaging time for PET). This resolution in turn provides the observation of localised perfusion defects which may otherwise be obscured. A further advantage of MRI is its ability to combine imaging of cardiac function, scar and other diagnostic targets into a single session, providing the potential to serve as a “one-stop shop” for cardiac diagnosis. And yet more, the zero ionising property makes MRI suitable for regular follow-up of patients.

### **3.2.6 Research Modalities**

Often in research applications, far greater image resolutions can be obtained when compared to clinical modalities since *ex vivo* techniques can be applied with extended imaging time. In terms of coronary anatomical imaging, vascular casting combined with high-resolution modalities has brought routine automation to what was once a labour-intensive task two decades ago. The imaging cryomicrotome, microCT and confocal microscopy all fall into this category, offering resolutions ranging from 1–25  $\mu\text{m}$  [92]. In terms of functional characterisation, it would appear that similar breakthroughs have yet to take place, and the microsphere injection technique [80] remains the gold standard for flow measurements in the myocardium.

### 3.3 Model Description

#### 3.3.1 Coronary Flow Modelling

As outlined in the previous sections, mathematical modelling of cardiac perfusion necessitates a multiscale framework. The anatomical and functional nature of cardiac perfusion means that no single modelling approach can accommodate all aspects of the integrated system. The series of models presented in this chapter aims to capture the dominant physical phenomena at each representative scale, guided by the need to simulate and predict clinically-relevant quantities. We emphasise, however, that our contribution is primarily directed at characterising the whole organ tissue perfusion and its surrogate measures observable in the clinics. This means that certain major aspects of coronary disease including fluid patterns in the presence of stenoses, and *in silico* FFR quantification, which require the determination of detailed localised flow dynamics will not be covered. Correspondingly, a framework to represent the 3D flow regime based on the Navier-Stokes equations is excluded. Nevertheless, there is a wealth of literature available on these topics, and the interested reader will find an entry point to the key contributions in [95] and references therein.

Wave propagation phenomena in the upper arterial vessels of the coronary network is an emerging clinical target which can be effectively addressed by a one-dimensional Navier Stokes flow model, at a fraction of the computational complexity of its 3D alternative. The key characteristics of the Stokes regime flow in the microvascular network can be captured by a porous media approach which bypasses the requirement for modelling individual vascular segments and allows for extended applications that informs protocols associated with non-invasive perfusion imaging. Such an approach also enables the natural extension of incorporating the effects of cardiac contraction via the poromechanical framework. A brief description of each of these models is provided in the following sections.

#### 3.3.2 1D Blood Flow Model

The physiological lengths of the coronary pulse waves are large compared to the vessels' diameters so that the wave propagation occurs mainly in the axial direction. The one-dimensional approximation is the preferred approach in network flow modelling since it can accurately reproduce the wave-propagation phenomena resulting from cardiac events, which cannot be accommodated by lumped parameter models. Furthermore, it affords numerical tractability in large multi-scale simulations where 3D Navier-Stokes becomes intractable [61]. The mathematical background behind the 1D blood flow formulation has been extensively described in literature both from a theoretical [43, 77] and computational [2, 33, 35, 85, 87] perspective. This framework has been widely applied for investigating wave propagation in the systemic arteries, as reviewed in [99], and has been validated both *in vitro* [64] and *in vivo* [83]. The application of the 1D blood flow framework to the coronary arteries is a relatively recent field [61, 89]. However, the suitability of this modelling approach has been

recently strengthened by *in vivo* validation in the left coronary circulation of animal subjects [69]. The following section provides an overview of the selected 1D blood flow modelling approach with brief comparisons to other options available in literature. We refer to more extensive reviews for further details [2, 35, 61, 99].

### 3.3.2.1 Modelling Framework

Each vessel of the coronary network is modelled as a one dimensional impermeable tube of length  $l$  with cross-sectional area  $A(x, t)$ , where  $A(x, t) = \int_S d\sigma$  is defined as the area of a generic cross section  $S$  along the axial coordinate  $x$ . The cross-sectional area is allowed to vary non-uniformly thus making  $A(x, t)$  both space- and time-dependent. The underlying assumption is that the local curvature is small enough so that the problem can be described in one spatial dimension [43, 77, 87, 89, 99]. Blood flow in the vessel is described as  $Q(x, t) = A(x, t)u(x, t)$ , where  $u(x, t) = \frac{1}{A(x, t)} \int_S \hat{u} d\sigma$  is the axial velocity averaged over the cross-sectional area. Radial velocity is assumed to be negligible compared to the axial component.

As reviewed previously [83, 99], circular cross-sectional areas and axisymmetry are assumed meaning that the axial velocity can be represented as a function of radius, space and time. Furthermore, the axial velocity is assumed to be the product of a radially-dependent profile function and a mean velocity component that is space- and time-dependent  $u(x, t)$ . Several different ways to model the velocity profile can be found in literature [99]. Our choice here is to model the velocity profile with a blunt shape based on experimental observations [89].

Blood is modelled as an incompressible Newtonian fluid such that density  $\rho$  and dynamic viscosity  $\mu$  can be considered constant at the scale considered here. In addition, flow is considered to be laminar due to the low Reynolds number throughout the coronary network in physiological conditions.

### 3.3.2.2 Governing Equations

The 1D blood flow equations can be derived from first principles [43, 77, 85, 99] or, alternatively, they can be obtained by averaging the 3D Navier-Stokes equations [89] over the cross-section of an axisymmetric circular cylinder. The equations have been widely described in literature [2, 35, 43, 77, 85, 89, 99]. They comprise statements of the conservation of mass and momentum which can be written as

$$\frac{\partial A}{\partial t} + \frac{\partial Q}{\partial x} = 0, \quad (3.1)$$

$$\frac{\partial Q}{\partial t} + \frac{\partial}{\partial x} \left( \alpha \frac{Q^2}{A} \right) + \frac{A}{\rho} \frac{\partial p}{\partial x} + \kappa \frac{Q}{A} = 0. \quad (3.2)$$

The unstressed area  $A_0$  can vary spatially to model a tapering geometry of a coronary vessel. The term

$$\alpha(x, t) = \frac{\int_S \hat{u}^2 d\sigma}{Au^2} \quad (3.3)$$



is a non-dimensional correction factor for momentum flux which accounts for the shape of velocity profile over the cross-sectional area. The variable  $\alpha$  is usually assumed to be constant since it leads to considerable mathematical simplifications [33,89,99]. In the results below we assume  $\alpha = 1.1$ , following [89], for all the results presented unless otherwise stated. The variable  $\kappa$  is obtained from the integration of the 3D incompressible Navier-Stokes equations and represents the viscous resistance of the flow per unit length of vessel [89].

To close the system of equations and solve for the three unknowns  $(A, Q, p)$ , a constitutive law, relating pressure to area, has to be introduced. Several different forms have been proposed in literature, mainly derived from a linear elastic shell model [61,99]. A commonly-employed example of these types of constitutive relations, used in our modelling framework, is of the following form

$$p = p_{ext} + \frac{\beta(x)}{A_0} \left( \sqrt{A(x)} - \sqrt{A_0(x)} \right), \quad (3.4)$$

where  $p_{ext}$  is an extravascular pressure and  $\beta(x) = \frac{4\sqrt{\pi}E(x)h(x)}{3}$  is a parameter both dependent on the Young modulus  $E(x)$  and the vessel wall thickness  $h(x)$  [5]. This relation assumes a static equilibrium in the radial direction of a cylindrical tube.

In the general case,  $p$  is spatially dependent through its dependence on the underlying variables i.e.  $p = p(\beta(x), A(x), A_0(x))$  such that

$$\frac{\partial p}{\partial x} = \frac{\partial p}{\partial \beta} \frac{\partial \beta}{\partial x} + \frac{\partial p}{\partial A} \frac{\partial A}{\partial x} + \frac{\partial p}{\partial A_0} \frac{\partial A_0}{\partial x} \quad (3.5)$$

should be taken into account for the vessel tapering and the spatial variation in material properties. Note that, as demonstrated in [33], additional terms can be included in the constitutive law to model the impact of wall inertia, viscoelasticity and longitudinal vessel pre-stress. However, these additional terms are generally assumed to have secondary effects and are difficult to parameterise thus they are not considered in the current modelling approach.

The solution system can be written in quasi-linear form as

$$\frac{\partial \mathbf{U}}{\partial t} + \mathbf{H}(\mathbf{U}) \frac{\partial \mathbf{U}}{\partial x} = \mathbf{B}(\mathbf{U}), \quad (3.6)$$

where  $\mathbf{U} = \begin{bmatrix} A \\ Q \end{bmatrix}$ , and the Jacobian  $\mathbf{H}(\mathbf{U})$ ,

$$\mathbf{H}(\mathbf{U}) = \frac{\partial \mathbf{F}}{\partial \mathbf{U}} = \begin{pmatrix} 0 & 1 \\ -\alpha \frac{Q^2}{A^2} + c^2 & 2\alpha \frac{Q}{A} \end{pmatrix}, \quad (3.7)$$

and the right-hand term  $\mathbf{B}(\mathbf{U})$ ,

$$\mathbf{B}(\mathbf{U}) = \begin{bmatrix} 0 \\ -\kappa \frac{Q}{A} - \frac{A}{\rho} \left( \frac{\partial p}{\partial \beta} \frac{\partial \beta}{\partial x} + \frac{\partial p}{\partial A_0} \frac{\partial A_0}{\partial x} \right) \end{bmatrix}. \quad (3.8)$$

In (3.7),  $c(x) = \sqrt{\frac{\beta}{2\rho A_0}} A^{\frac{1}{4}}$  denotes the wave propagation velocity.

The analysis of this characteristic system has been performed in literature, to which we refer for further details [33, 85, 87]. However, it is important to highlight that, under the necessary condition that  $A > 0$ , the equation system (3.6) has two real and distinct eigenvalues

$$\lambda_{1,2}(\mathbf{U}) = \alpha u \pm \sqrt{c^2 + \alpha(\alpha - 1)u^2}. \quad (3.9)$$

With the physiological condition  $c \gg u$ , (3.6) results in a hyperbolic system. This means that from each point of the computational domain, two characteristic curves originate, one directed towards the inlet and one towards the outlet of the vessel. As a consequence, an inflow and an outflow boundary conditions have to be specified.

From a numerical implementation point of view several different approaches have been pursued in literature, including second order Taylor-Galerkin schemes [33] and discontinuous Galerkin formulations [85, 87]. Our current model [60] is based on the spectral/hp elements scheme reported in [87]. The temporal discretisation has been performed with a Crank-Nicolson scheme, which is implicit and second-order accurate.

The numerical problem requires the specification of a full set of boundary conditions for (3.1)–(3.2) at the inlet and outlet, even if the differential problem requires only one physical boundary condition per boundary [33, 87]. To address this, the current implementation projects the differential equations along the outgoing characteristic curves [34], fully retaining the differential equations' non-linearities. Other approaches in literature rely on characteristic extrapolation [33, 85].

### 3.3.2.3 Network Formulation

The single-vessel formulation outlined above can be extended to a network of vessels by imposing suitable coupling conditions at the junctions. The junctions can either include [33] or ignore the impact of the branching angles, and be represented as a single point or a separate tract containing the branch [94]. Our modelling choice here is to represent junctions as a single point and to exclude the impact of the branching angles and momentum loss through junctions, since they play a minor role in the physiological range of pressure and velocity [33].

The coupling conditions imposed are based on physical conservation laws [33, 35, 60, 85, 87]. Under the assumption that no fluid can be stored in the junctions, the mass conservation equation in an  $n$ -vessel junction states that

$$\sum_j Q_j = 0, \quad j = 1 \dots n, \quad (3.10)$$

where  $Q_j$  denotes the flow into the junction from the  $j^{th}$  vessel. Imposing the conservation of total pressure across the junction according to Bernoulli's law

$$p_j + \frac{1}{2}\rho u_j^2 = p_{j+1} + \frac{1}{2}\rho u_{j+1}^2, \quad j = 1..n-1 \quad (3.11)$$

combined with the mass equation provides  $n$  equations in  $2n$  variables  $(A_j, Q_j)$ ,  $j = 1 \dots n$ . The remaining  $n$  equations are obtained by imposing the *compatibility equations* [34] which prescribe appropriate conditions on the characteristics.

### 3.3.2.4 Boundary Conditions

A key challenge in formulating the boundary conditions for the 1D system arises from the requirement that the complex physiological responses originating from outside the simulation domain must be adequately reproduced. A brief overview of the most commonly used types is provided here.

Due to the hyperbolic nature of the problem as highlighted in Sect. 3.3.2.2, both an inlet and an outlet boundary condition must be prescribed. For the inlet boundary condition two possible approaches include the straightforward prescription of a measured waveform (pressure or flow) or a lumped model of the heart [14, 57].

Outflow boundary conditions on the other hand have to reproduce the effects of the truncated vasculature distal to the terminal vessels of a model. The simplest distal boundary condition is to impose a given pressure or a pressure-dependent flow (resistive boundary condition) at vessel terminals, however this brings with it the undesirable effect of unphysiological numerical wave reflections in the computational domain [86, 107]. Reflections can be avoided altogether using a non-reflecting boundary condition where the backward-traveling wave is prescribed as zero [33], although this is also unphysiological as it assumes an outlet vessel of infinite length.

An improved physiological outflow boundary condition is provided by lumped parameter Windkessel models, which appropriately reproduces the input impedance measured in the epicardial arteries [57, 106, 107]. Windkessel models with different levels of complexity have been successfully used both in modelling the systemic arteries [2, 35, 99] as well as the coronary vasculature [57]. A Windkessel model composed of several resistance–compliance ( $R$ – $C$ ) components combined with a time-varying distal pressure has been coupled to a coronary epicardial network for validation purposes [69], showing good agreement with *in vivo* measurements.

On the other hand, the Windkessel model parameters for  $R$  and  $C$  of the truncated network are difficult to estimate from *in vivo* measurements due in part to the cardiac contraction. Furthermore the Windkessel model does not faithfully reproduce high-frequency flow features [106]. The poor performance of Windkessel models in the high frequency range has been addressed with impedance boundary conditions, calculated as the root impedance of structured networks distal to the modelled vascular segment [75, 103], yielding an improvement over the Windkessel approach. However, these types of boundary conditions give rise to additional derivation and implementation issue that are not always straightforward to apply, as highlighted in [61]. Significant work remains to be done to parameterise the Windkessel and impedance boundary conditions in the coronary circulation.

A further alternative approach to modelling outflow boundary condition is to use a tapering vessel, which reproduces a series of reflected waves similar to a distal

network [68]. Finally, in order to capture the spatial heterogeneity of flow in the distal circulation, the 1D blood flow model can be coupled to a 3D porous medium representing the distal circulation (see Sect. 3.3.3.3).

### 3.3.3 Regional Perfusion Modelling by Porous Media Flow

While appropriate for modelling flow within the systemic and major coronary arteries, the 1D flow model is unsuitable for whole-organ perfusion modelling for a number of reasons: (i) the level of discrete vascular detail acquired via clinical imaging modalities cannot resolve beyond the largest epicardial vessels; (ii) the large number of branching vessels represent a significant computational challenge even with a 1D formulation; and (iii) if the discrete network was not fully-formed (i.e. the entire network was described from arteries to veins, inclusive of the capillaries), then a large number of intramural terminal vessels would require the prescription of boundary conditions which are difficult, if not impossible, to determine.

In contrast, mathematical models of flow through porous media provide a promising alternative framework whereby the flow at the microvascular scale is approximated by a spatially-averaged flow on the macroscopic scale. In the context of perfusion modelling, it is generally assumed that the medium consists of two overlapping phases – the solid matrix and the fluid (pore space), each occupying a fraction of the volume at every point. In this work, we assume that the pore space is fully interconnected and saturated.

The most commonly applied porous media flow model is *Darcy's Law*, whereby the Darcy velocity,  $\vec{w}$ , is linearly proportional to the gradient of the fluid pressure,  $p$

$$\mathbf{w} + \mathbf{K} \cdot \nabla p = \mathbf{0} \quad \text{in } \Omega, \quad (3.12a)$$

$$\nabla \cdot \mathbf{w} = S_v \quad \text{in } \Omega, \quad (3.12b)$$

where  $\mathbf{K}$  is the permeability of the porous medium  $\Omega$ ,  $\rho$  denotes fluid density and  $S_v$  is a fluid volumetric source field. Darcy's Law has been used by previous perfusion models for biological tissues [17, 101]. Furthermore, the continuum approach has the additional advantage of matching the level of detail observable in clinical perfusion imaging which is inherently spatially-averaged, readily allowing comparison without ambiguity in postprocessing.

#### 3.3.3.1 Multi-compartment Static Darcy

In practice, when a vascular tree spanning a broad scale range is considered, the lumping of all pore spaces into a common compartment as represented by (3.12) becomes an inadequate assumption. These situations lead us to consider a multi-compartment extension of the model as outlined here.

From high resolution imaging studies of coronary anatomy, the close spatial proximity of vessels with widely-varying length and diameter scales is well-known [92] and would be expected to lead to a corresponding heterogeneity in pressure and flow.

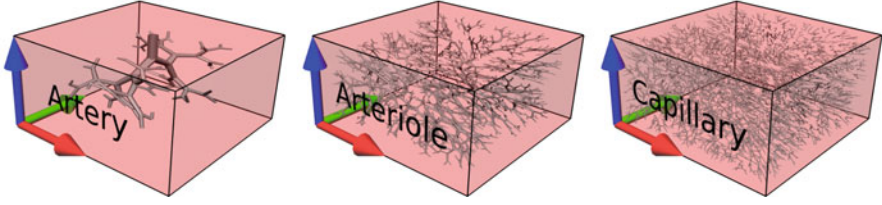


**Fig. 3.1.** Illustration of multiple spatially coexisting Darcy compartments. Each point of the physical domain  $\Omega$  will have a set of parameters and state variables for each compartment, with the particular parameters dependent on the vessels assigned to the compartment after vascular model partition. Note the decreasing scale of vessel in each compartment from *left* to *right*

Thus, to characterise the flow occurring within widely-disparate vessel scales, the approach taken below in our work is to employ *multiple* porous compartments, with each compartment representing a different range of vascular scale. Each compartment spatially coexists with all other compartments and occupies its own fractional volume (Fig. 3.1). Note that in perfusion modelling, the contribution of the interstitial volume is generally disregarded, due to the comparatively limited flux of fluid across the capillary membranes, and the slower diffusion-driven mode of transport in the interstitial space. The multi-compartment static Darcy system, and the methods used to parameterise the material properties of the porous domains, are presented below.

The multi-compartment Darcy system extends the single compartment Darcy model to  $N$  porous domains, and has been applied to previous perfusion modelling problems [21, 102]. The Darcy system for a compartment  $i \in [1, N]$  is (Einstein summation is not in use):

$$\mathbf{w}_i + \mathbf{K}_i \cdot \nabla p_i = 0 \quad \text{in } \Omega, \quad (3.13a)$$

$$\nabla \cdot \mathbf{w}_i = S_{v_i} - \sum_{k=1}^N \beta_{i,k} (p_i - p_k) \quad \text{in } \Omega, \quad (3.13b)$$

where subscripts  $i$  and  $k$  are compartment indices and  $\beta$  is a matrix of inter-compartment pressure-coupling coefficients. Note that  $\beta_{i,k} \in \mathbb{R}_0^+$  and  $\beta_{i,k} = \beta_{k,i}$  for  $i, k = 1, \dots, N$  in order to conserve fluid mass across the system. Eqs. (3.13) were set on an open bounded domain  $\Omega \subset \mathbb{R}^n$  with spatial dimension  $n$  and a piece-wise smooth boundary  $\partial\Omega$ , upon which zero flux boundary conditions were enforced.

As previously mentioned, the permeability tensor field  $\mathbf{K}$  contains the coefficients of proportionality relating the Darcy velocity  $\mathbf{w}$  to the pressure gradient. The permeability  $\mathbf{K}$  is a material property of the porous medium and it has the following key properties related to the physical constraints of the system [6]:

- $\mathbf{K}$  is symmetric, by the Onsager's reciprocal relation. This ensures that there is no bias in the material and a reversal in the pressure gradient should lead to a matching reversal in flow.

- $\mathbf{K}$  is positive definite. This property ensures that the direction of flow is always in the same direction as the pressure drop, i.e. fluid flows from region of high pressure to lower pressure.

### 3.3.3.2 Poroelasticity

The static Darcy perfusion model developed thus far lacks the ability to capture fluid-solid interactions as it assumes a rigid solid skeleton. In certain physiological applications, it is crucial to account for such interactions in order to capture the dynamics of the cardiac phase dependence of flow. For this reason, we now extend the porous flow framework to a general poromechanical one in which deformation of the medium and the resulting interactions with the pore fluid are defined. The application of poromechanical models in the context of perfusion in a contracting myocardium has been limited to a small number of studies to date [17, 44]. The comprehensive theoretical background can be found in [23, 24], which establishes a finite strain theory of poromechanics. Where applicable, we defer the description of specific constitutive relations and geometrical modelling choices employed to the results in Sect. 3.4.1.3.

#### Kinematics

In the poromechanical framework adopted here, a porous medium is treated as a superposition of solid and fluid continua, each occupying a fraction of the total volume at every point in the material. The smallest relevant unit of the material is termed a Representative Elementary Volume (REV), denoted as  $d\Omega$ , and contains a sufficient number of pores to allow a macroscopically averaged description. Thus an REV is not infinitesimal but must satisfy the requirement of being “small” relative to the total body, which is dependent on the particular problem under consideration. Note the standard terminologies *matrix* and *skeleton* indicate a distinction between the microscopic and macroscopic (averaged) solid phases, respectively.

The volume fraction occupied by the fluid is referred to as *porosity*, defined by  $\phi = \frac{d\Omega^f}{d\Omega}$  where superscript  $f$  refers to fluid. Fully saturated and connected pores are assumed in this work, which leads to the solid fraction being  $\phi^s = 1 - \phi = \frac{d\Omega^s}{d\Omega}$ , where  $s$  refers to solid. In the following, a Lagrangian reference frame (i.e. tied to the skeleton) is employed since skeletal deformation is most readily observable, and it leads to similar results familiar from existing work in cardiac mechanical modelling.

Briefly, a skeleton particle at position  $\mathbf{X}$  in the reference configuration is identified with the particle at deformed position  $\mathbf{x}$ , such that  $\mathbf{x} = \mathbf{x}(\mathbf{X}, t)$ . This leads to the standard definitions of deformation gradient  $\mathbf{F} = \nabla_{\mathbf{X}}\mathbf{x}$ , Jacobian  $J = \det(\mathbf{F})$ , and the right Cauchy-Green deformation tensor  $\mathbf{C} = \mathbf{F}^T \mathbf{F}$ . The Green-Lagrange strain tensor is then defined to be  $\mathbf{E} = \frac{1}{2}(\mathbf{C} - \mathbf{I})$ .

An alternative definition of  $J$  is expressed as  $J = \frac{d\Omega}{d\Omega_o}$ , where the subscript  $o$  refers to the reference configuration, and  $d\Omega$  now refers to the REV in the current configuration. In addition, because  $d\Omega$  in general changes with altered fluid content, the

change in pore volume is better captured by the *Lagrangian porosity*  $J\phi = \frac{d\Omega^f}{d\Omega_o}$ , which expresses the ratio of the current fluid content to the reference volume.

A common assumption made in cardiac mechanics is the incompressibility of the myocardial tissue. In the context of poromechanical models, however, such an assumption requires a further clarification. Considering the macroscopic skeleton to be an incompressible medium would be inappropriate as the net flow in and out of the tissue can always cause a bulk volume change. Rather, it is the solid matrix which we regard as incompressible. Assuming there is no solid mass creation occurring within the time scale under consideration, the conservation of solid phase can be written as

$$\rho^s(1 - \phi)d\Omega = \rho_o^s(1 - \phi_o)d\Omega_o \quad (3.14)$$

which, upon inserting the incompressibility condition of density  $\rho^s = \rho_o^s$ , can be expressed as

$$J - J\phi = 1 - \phi_o = \phi_o^s. \quad (3.15)$$

This can be contrasted with the hyperelastic incompressibility condition  $J - 1 = 0$ .

### Conservation Laws

The fluid continuity equation is expressed as

$$\frac{dm}{dt} + \nabla_{\mathbf{X}} \cdot (\rho^f \mathbf{W}) = S, \quad (3.16)$$

where  $m$  represents the current additional fluid mass content per unit reference volume, and  $S$ , a mass source term.  $\mathbf{W}$  is a Lagrangian counterpart to the Eulerian Darcy velocity  $\mathbf{w}$  which is now generalised to be

$$\mathbf{w} = \phi (\mathbf{v}^f - \mathbf{v}^s) = \phi \left( \frac{d\mathbf{x}^f}{dt} - \frac{d\mathbf{x}^s}{dt} \right). \quad (3.17)$$

The conservation of momentum is often described for the combined medium, such that

$$\nabla_{\mathbf{X}} \cdot (\mathbf{F}\mathbf{S}) + m^s(\mathbf{f} - \mathbf{a}^s) + m^f(\mathbf{f} - \mathbf{a}^f) = 0, \quad (3.18)$$

where  $\mathbf{S}$  represents the second Piola-Kirchhoff stress, and  $\mathbf{f}$  and  $\mathbf{a}$  represent body force density and acceleration, respectively. Variables  $m^s$  and  $m^f$  can be regarded as density-like quantities which denote respectively the skeletal and fluid mass content per unit reference volume. Note that  $m^f$  and  $m$  are related via

$$m^f = \rho_o^f \phi_o + m. \quad (3.19)$$

### Constitutive Relation

Formulation of a constitutive relation for an open porous medium involves many challenges. Thermodynamic considerations can help to identify appropriate state variables and equations which are consistent with the assumptions made for a specific medium. In a continuum mechanics framework the entropy condition is expressed by the Clausius-Duhem inequality, the general expression for a porous

medium of which is [27]

$$D = \mathbf{S} : \frac{d\mathbf{E}}{dt} + p \frac{d(J\phi)}{dt} - S \frac{dT}{dt} - \frac{d\Psi^s}{dt}, \quad (3.20)$$

which states that the intrinsic dissipation  $D$  is dependent on both skeletal and pore strain work rates and entropy variation. Here,  $S$  and  $T$  denote entropy and temperature respectively and  $\Psi^s$  denotes the Lagrangian free energy density of the skeleton. In cardiac modelling, further simplification can be made if we assume the myocardial tissue to be an isothermal, *poroelastic* medium, for which dissipation is zero, yielding

$$\frac{d\Psi^s}{dt} = \mathbf{S} : \frac{d\mathbf{E}}{dt} + p \frac{d(J\phi)}{dt} \quad (3.21)$$

giving the state equations

$$\mathbf{S} = \frac{\partial \Psi^s}{\partial \mathbf{E}}, \quad p = \frac{\partial \Psi^s}{\partial (J\phi)} \quad (3.22)$$

stating that  $\mathbf{S}$  and  $p$  respectively are the thermodynamic forces driving the changes in  $\mathbf{E}$  and  $J\phi$ .

Additional requirements can be posed on the general form of the free energy function  $\Psi^s(J\phi, \mathbf{E})$  to address the cases when the porosity reaches the physical limits of 0 or 1. However, in the incompressible regime, (3.15) implies that  $\phi < 1$  for  $0 < J < \infty$ , thus we focus our attention on the compaction limit ( $\phi \rightarrow 0$ ). Following [30], an effective barrier potential would remain inactive (contributes zero pressure and stiffness) until compaction is approached, but once activated, provides pressure and stiffness which tend toward infinity thus preventing further extraction of the pore fluid. Thus we seek to construct a barrier potential  $\Theta(J\phi)$  which satisfies

$$\frac{\partial \Theta}{\partial (J\phi)} = \frac{\partial^2 \Theta}{\partial (J\phi)^2} = 0, \quad \text{for } J \geq 1, \quad (3.23)$$

$$-\frac{\partial \Theta}{\partial (J\phi)} \rightarrow +\infty, \quad \text{for } J\phi \rightarrow 0, \quad (3.24)$$

$$\frac{\partial^2 \Theta}{\partial (J\phi)^2} \rightarrow +\infty, \quad \text{for } J\phi \rightarrow 0. \quad (3.25)$$

This leads to the general form of free energy

$$\Psi^s = \Phi(\mathbf{E}, J\phi) + \Theta(J\phi). \quad (3.26)$$

As there is substantial work still to be undertaken in designing and validating a specific cardiac poroelastic constitutive law, at this stage we propose a further decomposition of  $\Psi^s$  such that

$$\Psi^s = \bar{\Phi}(\mathbf{E}) + \hat{\Phi}(J\phi) + \Theta(J\phi) \quad (3.27)$$

which enables the previously characterised hyperelastic constitutive laws and coronary pressure-volume relationships to be substituted.



In addition, in a contracting myocardium the stress tensor is augmented by an active component such that

$$\mathbf{S} = \mathbf{S}_p + \mathbf{S}_a \quad (3.28)$$

where  $\mathbf{S}_p$  and  $\mathbf{S}_a$  represent the passive and active components, respectively. The active stress is assumed to act along the fibre direction  $\mathbf{f}$  in the deformed configuration, thus yielding the active component of the Cauchy stress tensor

$$\boldsymbol{\sigma}_a = T_a \mathbf{f} \otimes \mathbf{f} \quad (3.29)$$

which is related to the second Piola–Kirchhoff stress tensor via

$$\mathbf{S}_a = J \mathbf{F}^{-1} \boldsymbol{\sigma}_a \mathbf{F}^{-T}. \quad (3.30)$$

The fibre active stress  $T_a$  is calculated by an auxiliary model of time-dependent fibre stress development and  $\mathbf{f}$  denotes the deformed fibre axis direction. The specific relations we have used to represent the components of the constitutive law are outlined in Sect. 3.4.1.3.

### 3.3.3.3 Vascular-porous Medium Coupling

For applications that warrant subject-specific anatomy, coronary-contraction coupling or involve integrative physiological mechanistic investigations, combining the 1D framework with the porous approach may be instrumental. The 1D–3D coupling can also address the problem of potentially reversing inflow boundary conditions in the porous domain, and more accurately represent the distal mechanical interactions responsible for wave generation, thereby helping to overcome the shortcomings in each respective model.

Anatomically, the interface domain between the explicit proximal vascular segments and porous medium consists of meso-scale arterioles which transition into the microcirculation over several bifurcating generations. Therefore, instead of treating the interface as a point-to-point coupling – which would result in concentrated tissue inflow and thus unphysiological pressure peaks – we assume that the exchange of fluid between a vessel terminal and the porous tissue occurs in a distributed manner over the volume  $\Omega_{int}$  in the neighbourhood of the terminal, such that

$$\rho^f Q_{1D}(t) = \int_{\Omega_{int}} S(\mathbf{x}, t) d\Omega. \quad (3.31)$$

For clarity, variables in the 1D flow model are denoted with a subscript 1D here. We choose to express  $S$  via a distribution function  $f$  such that

$$S(\mathbf{x}, t) = \rho^f Q_{1D}(t) f(\mathbf{x}) \quad (3.32)$$

which, together with (3.31) implies that

$$\int_{\Omega_{int}} f(\mathbf{x}) d\Omega = 1 \quad (3.33)$$

must be held. The pressure–flow relationship of the coupling interface is described by observing that the meso-scale vessels are predominantly resistive elements comprising thick-walled arterioles, leading to

$$Q_{1D}(t) = \frac{p_{1D}(t) - \bar{p}(t)}{R_{meso}} \quad (3.34)$$

where  $R_{meso}$  is the resistance of the coupling interface. As a first approximation, we define the average pore pressure  $\bar{p}$  as

$$\bar{p} = \int_{\Omega_{int}} p(\mathbf{x}, t) f(\mathbf{x}) d\Omega. \quad (3.35)$$

The coupling problem therefore seeks to find values of  $Q_{1D}$  and  $p$  which satisfy (3.34) and (3.35). Several strategies can be envisioned to specify the function  $f(\mathbf{x})$ , including an analytic derivation from an assumed branching structure, or directly characterised from detailed network morphology. In the absence of such data however, we employ a simpler approach in this work and approximate  $f$  with a Gaussian function. To ensure (3.33) holds,  $f$  is formulated as

$$f(\mathbf{x}) = \frac{1}{\int_{\Omega_{int}} G(\mathbf{x} - \mathbf{x}_{term}) d\Omega} G(\mathbf{x} - \mathbf{x}_{term}) \quad (3.36)$$

where  $\mathbf{x}_{term}$  denotes the position of the vessel terminal, and  $G$  is a standard Gaussian kernel.

### 3.3.3.4 Parameterisation of Porous Medium

We now depart from the largely theoretical focus examined up to this point and briefly consider the issue of characterising the porous medium parameters from real-world data. This will assist in addressing questions such as whether the continuum approach is a suitable one for modelling coronary network flow, and how a detailed anatomical network morphology can be condensed into equivalent porous medium parameters. The methods outlined below necessitates the use of high-resolution animal data, but in exchange offers the means by which to determine the appropriate parameter ranges in health and disease, as a basis for extrapolation to humans as is common in medical research. Further discussions on clinical translational strategies are provided in Sect. 3.5.

Models of the discrete vascular network reconstructed from high-resolution imaging data [100] are well-suited for the distillation of important microvascular characteristics into continuum parameters. To enable the parameterisation of the individual compartments, one must first compartmentalise (or longitudinally partition) the vascular model. The so-called *hierarchical parameter* vascular model field is used for this purpose. This is a monotonically decreasing field with respect to a proximal-distal direction of flow, with the value 1 at the proximal node of the network, 0 at all distal terminal nodes, and the value of the summed length of all distal vessels at intermedi-

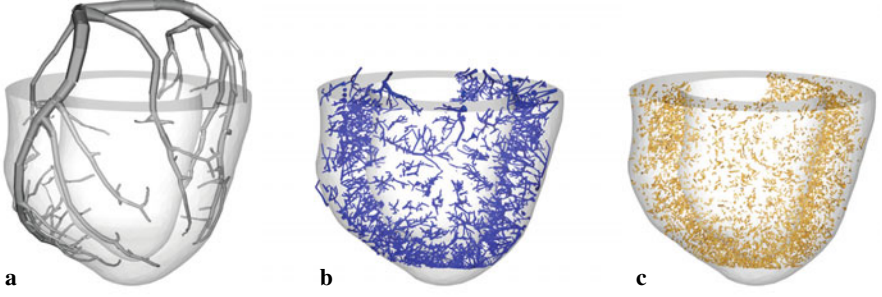


**Fig. 3.2.** Compartmentalisation of a porcine arterial network derived from cryomicrotome data. This example, which assumes two Darcy compartments, consists of (a) the 1D portion which drives the fluid flow in the continuum model, and the compartment 1 and 2 discrete vessels that will be spatially-averaged into macroscale continuum permeability parameters ((b) and (c), respectively)

ate nodes divided by the summed length of all vessels. Note that pressure solutions from a discrete flow model have also been previously applied to define the hierarchic parameter field [102]. This robust partitioning metric preserves the “natural order” of flow, i.e. proximal vessels are allocated to proximal Darcy compartments. Ultimately the particular hierarchic parameter values that dictate the vascular partition must be selected on an application-dependent basis. For instance, Fig. 3.2 shows an example compartmentalisation of a porcine arterial model for use in parameterising a two-compartment porous perfusion model. For simplicity of this illustration, an approximate equal split in the number of vessels to be spatially-averaged between Darcy compartments 1 and 2 was applied.

Once compartmentalised, spatial-averaging techniques (using an averaging window of constant size, denoted  $d\Omega$ ) are employed to extract the effective parameter fields, such as the porosity of compartment  $i$ , defined to be

$$\phi_i(x) = \frac{\sum_{v \in V_i(x)} vol_v}{vol_{d\Omega}}, \quad (3.37)$$

where  $V_i(x)$  is the set of vessels assigned to Darcy compartment  $i$  within the averaging volume centered at a point  $x \in \Omega$ , and  $vol_\varepsilon$  is defined as the volume of a domain  $\varepsilon$  that intersects  $\Omega$ . Thus the total porosity of the material is

$$\phi(x) = \sum_{i=1}^N \phi_i(x). \quad (3.38)$$

Importantly, we use a discrete Poiseuille flow model solution to produce local variables that are dependent on the entire network topology. Specifically, the Poiseuille pressure at a node in the discrete vascular model is calculated using the Poiseuille network matrix [79]. Note that the pressure derived from the linear Poiseuille model is also dependent on the boundary conditions applied. However we have pre-

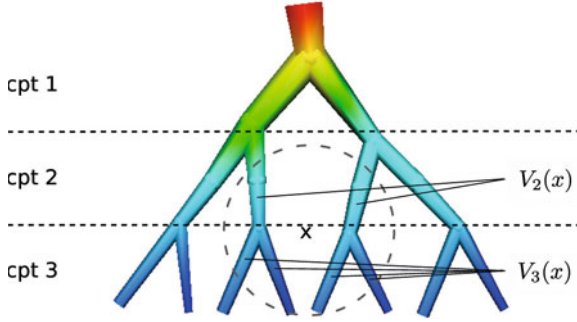


**Fig. 3.3.** Schematic of a simple network to illustrate the vessels involved in parameterising the continuum permeabilities at a point  $x$ . The averaging window is delineated by the dashed circle, with centrepoint  $x$  ( $x$  is typically a finite element mesh node). Note that for this example point,  $V_1(x)$  and the compartment-connecting vessel sets  $c_{1,2}(x)$  and  $c_{1,3}(x)$  are equal to the null set, whereas  $c_{2,3}(x) = V_2(x)$  as both vessels in  $V_2(x)$  are connected to vessels in  $V_3(x)$

viously shown the robustness of using the Poiseuille model to characterise flow parameters with respect to varying boundary conditions [47]. Thus, we define the spatially-averaged discrete pressure for vessels in the  $i^{\text{th}}$  compartment to be

$$\bar{p}_i(x) = \frac{\sum_{v \in V_i(x)} P_v \text{vol}_v}{\sum_{v \in V_i(x)} \text{vol}_v}, \quad (3.39)$$

where  $P_v$  is the averaged discrete pressure (mean of the two nodal values) for the  $v^{\text{th}}$  vessel within  $V_i(x)$ , and  $\Delta p_v$  is the difference in pressure across the vessel.

The discrete mass flux between compartments is a key variable in the evolution of multi-compartment porous flow. The set of all vessels within  $d\Omega$  that belong to compartment  $k$  but share a node with a compartment  $i$  vessel is denoted by  $c_{i,k}$  (see Fig. 3.3 for a schematic illustrating these sets of compartment-connecting vessels). The flux from compartments  $i$  to  $k$  is then

$$Q_{i,k}(x) = \sum_{v \in c_{i,k}(x)} \frac{\pi r_v^4}{8\mu l_v} (\Delta p_v). \quad (3.40)$$

From the perspective of the Darcy model,  $\beta_{i,k}$  can be viewed as the local constant of proportionality between the fluid flux transfer and the difference in the Darcy pressures. Thus, we use the data derived from the discrete model to define these continuum fields via

$$\beta_{i,k}(x) = \begin{cases} 0 & \text{if } \bar{p}_i(x) - \bar{p}_k(x) = 0. \\ \frac{Q_{i,k}(x)}{|\bar{p}_i(x) - \bar{p}_k(x)|}, & \text{otherwise.} \end{cases} \quad (3.41)$$

Unsurprisingly, these inter-compartment coupling fields play a major role in determining the overall fluid flow within the model, due to their widespread heterogeneity

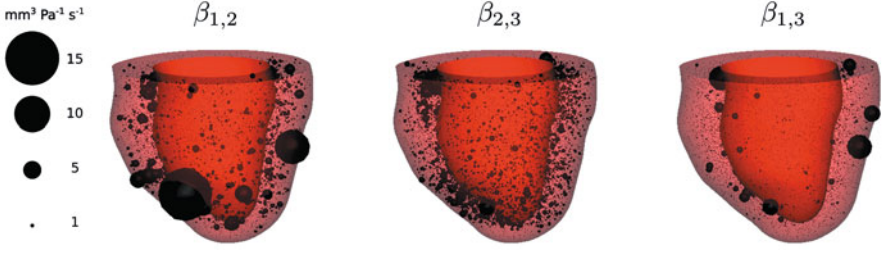


**Fig. 3.4.** The spatial distribution of the continuum  $\beta$  fields allows for heterogeneous mass transfer amongst compartments. Here we consider a three-compartment Darcy model, where the left ventricular endocardial surface is opaque while the epicardial surface is transparent. Each finite element mesh node is represented by a spherical glyph whose diameter is equal to the  $\beta$  value at that node. Note in particular the heterogeneous  $\beta_{1,3}$  field, which illustrates the level of non-adjacent compartment coupling in this  $N = 3$  model scenario

and the presence of “long-range” coupling, i.e. coupling between non-neighbouring compartments (Fig. 3.4).

Finally, we present two methods which may be applied to parameterise the permeability tensor fields, depending on the level of discrete data available. The simpler method is to assume a porosity-scaled isotropic permeability, i.e.

$$K_i(x) = c_{Ki}\phi_i(x)I, \quad (3.42)$$

where  $I \in \mathbb{M}_{3 \times 3}$  is the identity tensor with assumed units of  $\text{mm}^2 \text{Pa}^{-1} \text{s}^{-1}$ , and  $c_{Ki}$  is a constant scaler of the permeability which is solved for in a post-processing minimisation problem to best match the continuum pressures with the spatially-averaged discrete pressures [46]. Alternatively, one can use a previously proposed method [45] whereby the permeability tensor is defined as

$$K_{ij} = \frac{\pi}{128 \text{vol}_{d\Omega} \delta x_0 \mu} \sum_{ns} \frac{d_{ns}^4 \Delta x_{ns,i} \Delta x_{ns,j}}{l_{ns}}, \quad i, j = 1, 2, 3, \quad (3.43)$$

with  $\delta x_0$  being an infinitesimal element of their hierarchic parameter,  $ns$  is the set of vessels within the hierarchic parameter range  $\delta x_0$ ,  $d$  is the vessel diameter, and  $\Delta x_{ns,i}$  is the absolute difference in spatial coordinate  $i$  between the vessel end points.

### 3.4 Model Applications

In this section we present clinically-oriented applications of the modelling framework described in the previous sections. Selected examples include a model for *in silico* wave intensity analysis featuring varying degrees of complexity, and a myocardial transport model for calculating contrast agent dynamics. The reduced complexity WIA model is aimed particularly at time-bound interventional clinical settings, whereas the full poroelastic model enables the interpretation of limited data

collectable in these situations through mechanistic investigation unachievable with the simpler model. These examples illustrate our efforts to address real-world problems in which the quantity of observable data and time constraints play a significant role in directing the appropriate modelling approach. The transport model, on the other hand, allows the perfusion simulations to be compared directly with clinically-acquired data, thus closing the loop between modelling and imaging. Taken together, these applications focus on assessing the combined states of myocardial perfusion and function.

### 3.4.1 Coronary Wave Intensity Analysis

Due to the technological advancements over the past decade in coronary catheter wires which enabled simultaneous measurements of pressure and velocity, wave intensity analysis (WIA) has emerged as a useful tool with which to study the underlying cardiac and hemodynamic function. Its application to the human coronary system has identified six major waves, each attributed to different events of the cardiac cycle [25], the characteristics of which are now being applied for clinical diagnosis. Simultaneous measurements of pressure and velocity acquired *in vivo* in a human LAD are shown along with the calculated WIA in Fig. 3.5 for illustrative purposes.

#### 3.4.1.1 Theoretical Background

This section outlines the mathematical background for calculating wave intensity from coronary waveforms. For an in-depth theoretical and practical discussion, we refer the readers to a recent review [76]. The catheter-acquired pressure and velocity raw data in the clinic are ensemble averaged and then smoothed using the Savitzky-Golay filter. The time derivatives of the pressure and velocity signal can be obtained directly from the filter or estimated as the time increments of the smoothed pressure  $p(t)$  and velocity  $u(t)$  signals, as

$$dp = p(t + dt) - p(t), \quad du = u(t + dt) - u(t), \quad (3.44)$$

where  $dt$  indicates the sampling time. Using the water hammer equations, relating changes in velocity and change in pressure in a wavefront

$$dp_+ = \rho c du_+ \quad \text{for forward travelling waves} \quad (3.45)$$

$$dp_- = -\rho c du_- \quad \text{for backward travelling waves} \quad (3.46)$$

where  $\rho$  denotes fluid density. It is then possible to compute the wave intensity as

$$dI(t) \equiv \frac{dp(t)}{dt} \frac{du(t)}{dt}. \quad (3.47)$$

Dividing the time increments by  $dt$  avoids the dependence of WIA on the sampling time step size. The fundamental property of wave intensity is that at each sampling point of the measured waveform,  $dI(t)$  highlights if the forward or backward trav-

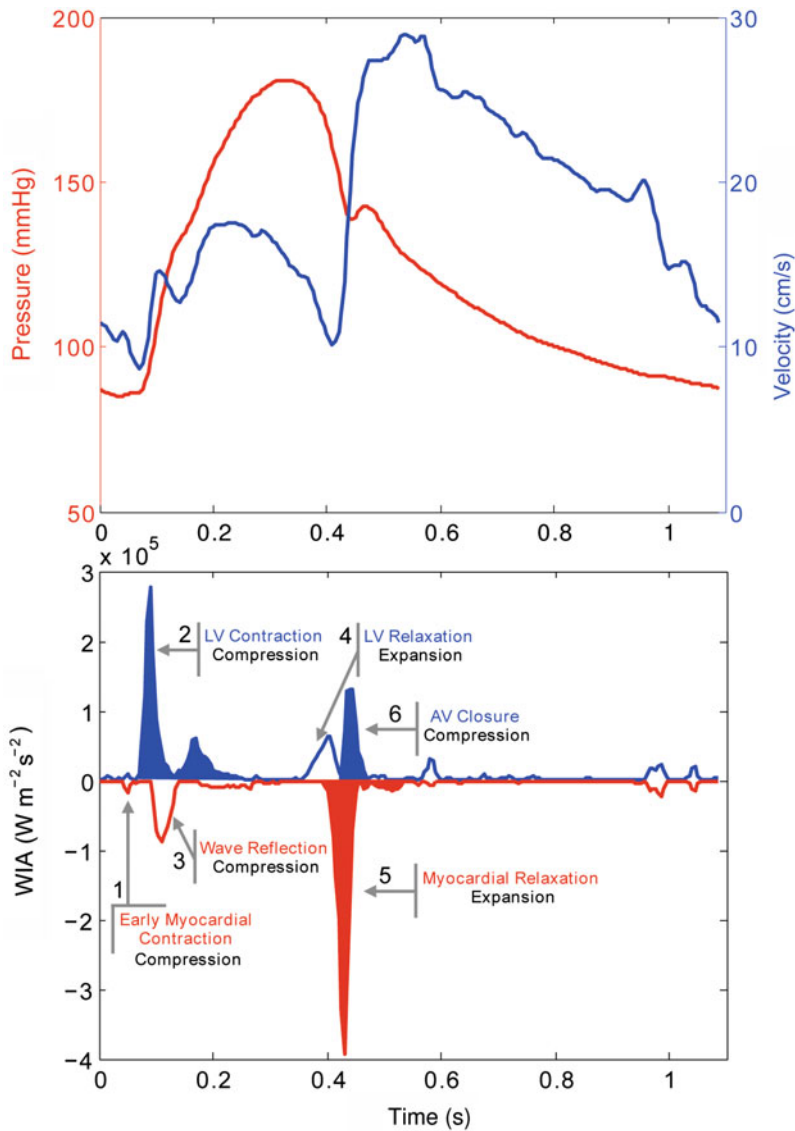


**Fig. 3.5.** The pressure and velocity signals, acquired *in vivo* in a human subject, have been ensemble-averaged over 9 beats (*top*). The resulting forward and backward separated waves are shown (*bottom*). For each of the major waves the related cardiac event and the associated change in coronary pressure are highlighted (compression=increase, expansion=decrease). The coloured waves are associated with flow acceleration whereas the uncoloured ones indicate flow deceleration. The waves have been numbered following [25]. It is important to highlight that the wave 1 is not always detectable due to the relatively low amplitude. AV = aortic valve, LV = left ventricle

elling wave is dominant at that instance. With the further assumption that forward and backward travelling waves sum linearly when interacting

$$dp = dp_+ + dp_- , \quad du = du_+ + du_- , \quad (3.48)$$

combined with (3.45), it is possible to separate the simultaneous forward and backward travelling waves

$$dI_{\pm} \equiv \frac{dp_{\pm}}{dt} \frac{du_{\pm}}{dt} = \pm \frac{1}{4\rho c} \left( \frac{dp}{dt} \pm \rho c \frac{du}{dt} \right)^2 , \quad (3.49)$$

where

$$dp_{\pm} = \frac{1}{2}(dp \pm \rho c du), \quad du_{\pm} = \frac{1}{2} \left( du \pm \frac{dp}{\rho c} \right). \quad (3.50)$$

The pulse wave speed (PWS) of the coronary vessel ( $c$ ) is then usually estimated by using the sum-of-squares method [1, 25]

$$c = \frac{1}{\rho} \sqrt{\frac{\sum dp^2}{\sum du^2}}, \quad (3.51)$$

which is to date the only single point method published. It is important to stress that the summations have to be taken over an integer number of cardiac cycles. Finally, the separated component of pressure and velocity can be computed as follows

$$p_{\pm}(t) = \sum_0^t dp_{\pm}(t) + p_0, \quad u_{\pm}(t) = \sum_0^t du_{\pm}(t) + u_0, \quad (3.52)$$

where  $p_0 = p(t=0)$  and  $u_0 = u(t=0)$ .

### 3.4.1.2 Physiological Applications

Applying the theoretical framework outlined in Sect. 3.4.1.1, the key question we seek to answer first is whether or not the one-dimensional coronary model, presented in Sect. 3.3.2, can appropriately capture the epicardial flow and reproduce the main waves of the WIA profile. To address this question the model setup combines a patient-specific geometry and a RCR Windkessel boundary condition with a time-varying distal pressure (representing the LV pressure impact), as previously applied in [57, 69].

The motivations behind this modelling setup are practical. Firstly, if interventional clinical translations are of interest then the computation of the model must be fast. Secondly, the model inputs are constrained by the data available in the clinic, commonly limited to simultaneous single-point pressure and velocity measurements, at times augmented by the geometry of the large epicardial vessels or their 2D projection.

Despite its simplicity, this approach retains its clinical relevance as the measured waveforms can be fitted to estimate the Windkessel parameters (R-C) providing in-



formation about the distal vasculature. Moreover, when applied to healthy and diseased vessels, deviation in the estimated distal parameters can complement the information available in the clinical setting. Furthermore, a template distal time-varying pressure can be fitted to the measured data, providing an estimate of the left ventricular pressure which is highly desirable but usually inaccessible in the clinical diagnosis.

In an illustrative simulation below, the patient-specific geometry and the inlet and outlet area of the left anterior descending artery (LAD) were extracted from CT data and meshed using spectral elements of 5<sup>th</sup> order [87]. The LAD was assumed to taper linearly. The pressure and velocity waveforms were simultaneously measured using a dual pressure and Doppler sensor (Combwire, Volcano Corp). The PWS of 23 m/s was estimated using the sum-of-squares method (3.51) and  $\beta$  was adjusted such that the PWS is constant throughout the whole vessel (implying constant distensibility [83]). The inlet boundary condition was prescribed to be the pressure measured in the proximal part of the LAD. The values of the distal boundary condition parameters  $R_t = R_1 + R_2 = 4.5 \cdot 10^9 \text{ Pa} \cdot \text{s/m}^3$  and  $C = 0.625 \cdot 10^{-12} \text{ m}^3/\text{Pa}$  are within the physiological range found in literature [57, 83]. The scaled left ventricular pressure and the outlet boundary condition parameters were adjusted to obtain physiological flow. The model was run for several cardiac cycles until periodic flow was achieved.

Physiological coronary pressure and velocity profiles were obtained (shown in Fig. 3.6). Major features of the velocity waveform such as the early-systolic and late-systolic minima [68] and the sharp diastolic rise were represented in the simulated results. The modelled velocity profile (Fig. 3.6) qualitatively reproduces the measured data (from a different patient) shown in Fig. 3.5, demonstrating the capacity of the framework to capture the main features of wave propagation in a coronary vessel. (Direct comparison between the simulated and the measured velocity waveform in the same patient has not been possible due to the poor quality of the acquired velocity data in this case.)

The spatial variation in the velocity profile between the proximal and distal part of the LAD qualitatively follows the expected changes, as measured in [53]. The main relative variations between the proximal and distal velocities are an increase in the early-systolic negative velocity and a less evident early-systolic peak (at  $t \approx 0.1 \text{ s}$ ) and late-systolic minima (at  $t \approx 0.38 \text{ s}$ ), as described in [53].

In the current simulation setup, the calculated distal velocities are higher than in the patient due to the absence of side branches in the model. There are several practical considerations associated – with the current imaging technology, the clinically observable number and length of side branches are inconsistent across the patients and depends strongly on the image quality. If we were to model every observable side branch it will multiply the number of boundary Windkessel models, preventing a standardised interpretation of these parameters and their comparison across a population. Furthermore, the relative magnitudes of the main waves can be considered to be of greater clinical interest than the absolute values. In light of the inter- and intra-patient variabilities and the effect of autoregulation on basal flow and pres-

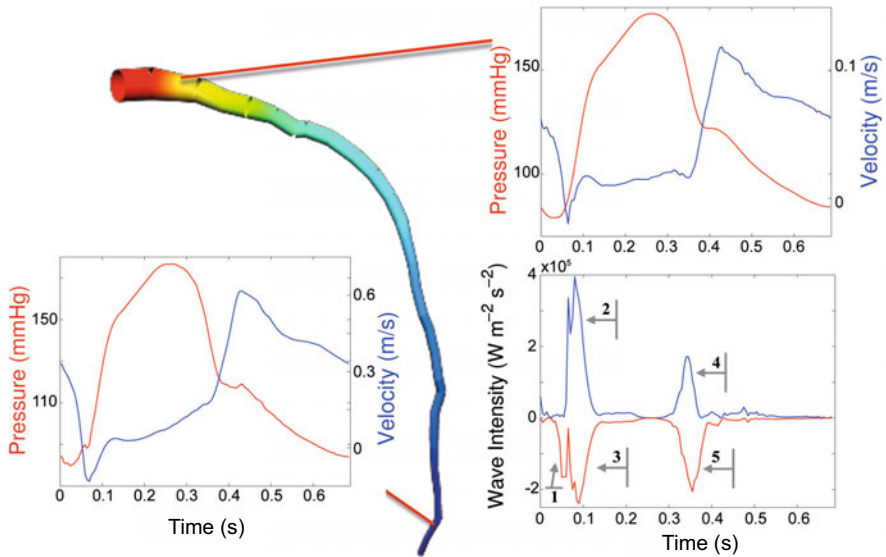


**Fig. 3.6.** The pressure and velocity waveforms in the proximal part of the LAD are visualised along with the coronary WIA profile, where the main waves of the coronary WIA profile [25] are clearly visible. The waves have been numbered following Fig. 3.5. The wave associated to the aortic valve transition is not reproduced, as the valve behaviour at the inlet was not included in the model

sure, the absolute wave intensity magnitude is uninformative unless acquired under several well-defined conditions and compared, thereby limiting its utility.

In conclusion, this model can be used to realistically reproduce the coronary WIA (cWIA), as shown in Fig. 3.6, as well as to investigate the impact that distal parameters (R, C or left ventricular pressure) have on the cWIA outcome. Moreover, by applying this model in an inverse manner, the underlying parameters of the model can be estimated as surrogate measures of distal vascular bed resistance and compliance. However, it is not suitable for investigating the link between each different wave and the mechanisms behind its origin, motivating the modelling approach presented in Sect. 3.4.1.3. Nevertheless, this application of the one-dimensional modelling reaffirms its ability to correctly reproduce wave propagation phenomena, even in the coronary epicardial vessels that are relatively short ( $\approx 10$  cm) with respect to the measured PWS ( $\approx 15$ -25 m/s).

### 3.4.1.3 Wave Intensity and Integrated Cardiac Function

Recent clinical research has shown that a coronary WIA-derived index can predict functional recovery following a myocardial infarction [26], demonstrating the clinical potential of the approach. However, a systematic investigation of the modulating

factors underlying each wave is currently not available. While such a study would be instrumental in advancing our prognostic capabilities through further mechanistic understanding, at present experimental options are limited due to the physiological complexity of the system under study. Detailed biophysical modelling on the other hand offers the possibility to establish quantitative and mechanistic linkages between cardiac function and the observed coronary waves, through parameter sensitivity analyses.

Here we present an integrative framework aimed at enabling an *in silico* WIA. It combines the one-dimensional vascular flow representation with a model of contracting myocardium that incorporates the poromechanical framework outlined in Sect. 3.3.3.2. The coupling between the two systems occurs both distally, at vascular termini distributed throughout the myocardium, and proximally, via the aortic sinus hemodynamics described as part of the reduced-order systemic circulation model. Rather than prescribing measured quantities as boundary conditions, the components of the model interact with one another and drive the evolution of the coronary waves, thus allowing mechanistic investigations of wave generation. The inlet pressure of the coronary system is determined by the aortic sinus pressure in the systemic circulation model, which in turn depends on the outflow from the left ventricle. Mechanical stress generation in the myocardium due to passive filling or the contractile forces contributes to the pore fluid pressure, which in turn feeds back onto the vascular flow. This framework thus allows the coupled wave propagation–perfusion–contraction dynamics to be studied throughout the full heart cycle.

The poroelastic constitutive relation (3.27) was composed of:  $\bar{\Phi}$ , an existing hyperelastic formulation of cardiac tissue [41] supplemented with a linearly viscoelastic term; and  $\hat{\Phi}$ , an adapted coronary pressure-volume relationship characterised from experimental measurements [13]. The compaction barrier potential  $\Theta$  was based on a functional form proposed in [30]. Active tension generation in the myofibres was modelled using a previously proposed relation employed for patient-specific modelling [71], which is a reduced-parameter formulation of [56].

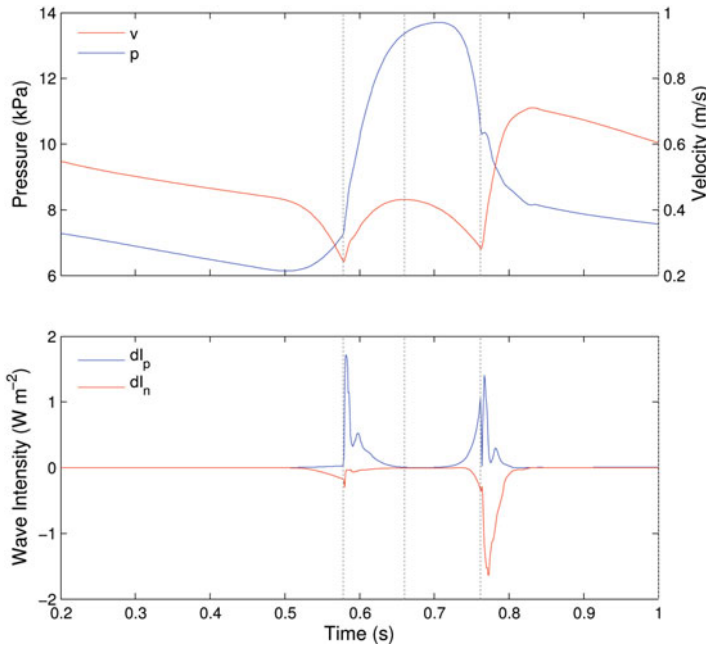
The resulting poroelastic problem was discretised using a Galerkin finite element formulation, with quadratic and linear hexahedral elements for displacement and pressure fields, respectively. The incompressibility constraint (3.15) was addressed via Lagrange multipliers. The 1D vascular flow problem was discretised using a 5th order spectral element basis. Time discretisation was performed using a Crank-Nicolson scheme. The resulting system comprised three sub-problems (poroelasticity (3.16),(3.18) vascular flow (3.1),(3.2) supplemented by the 1D-3D coupling (3.34),(3.35), and systemic windkessel) which were solved via a sequential fixed-point approach, ensuring nonlinear convergence at each time step.

The results are demonstrated on a porcine cardiac geometry obtained via high-resolution cryomicrotome imaging [92], from which the myocardial mesh and a truncated vascular mesh featuring 4000 vessels were obtained. After pre-processing, around 2000 vascular-myocardial coupling interfaces remained, distributed throughout the myocardium. The diameter of the truncated terminal vessels were approxi-

mately  $200\mu m$ . Because the terminal generation of vessels extended to the level of microcirculation in this case, for the current application a single porous compartment was considered adequate. Boundary conditions applied to the myocardium include a viscoelastic support at the base and elastic support over the epicardial surface. The porous medium outflow condition was determined by a distributed resistance reflecting distal vessels. The boundary conditions on the vascular problem was completely defined proximally by the coupling to aortic pressure, and distally by the 1D-3D coupling.

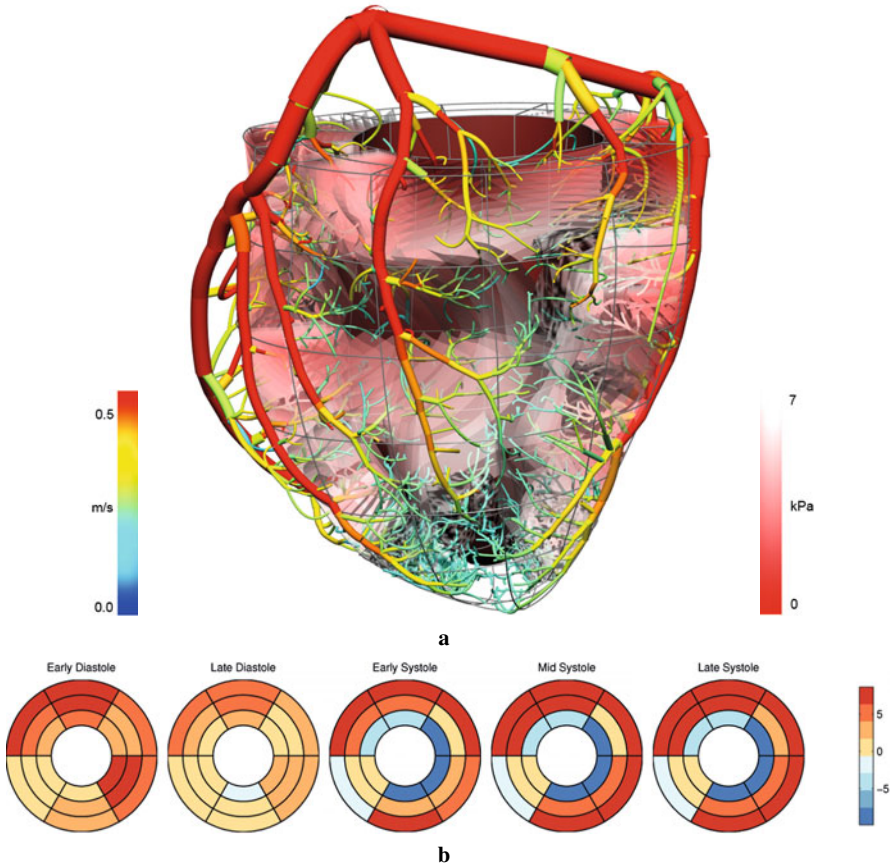
Simulations were performed with CHeart [58], an mpi-based parallel multiphysics solver developed at King's College London. The full set of model parameters and discussions of the results can be found in [59], and expanded descriptions on the employed numerical algorithms in [58].

Figure 3.7 shows an example of the physiological wave intensity profiles reproduced by the model. The dominant forward compression and backward expansion waves are accurately reproduced, as well as the smaller waves which occur during early diastole and late systole. Parameter perturbation analysis revealed key cardiac event-wave associations including a strong dependence of the forward compression wave (2) on the myocyte tension development rate, and the dominant backward expansion wave (5) on QRS duration and vascular resistance. The late forward com-



**Fig. 3.7.** Coronary pressure, velocity and wave intensity profiles from the integrated perfusion model. The results were sampled from a mid-LAD region. Good qualitative reproduction of the major forward and backward waves can be observed. For further discussion, refer to text

pression wave (6) was observed to exhibit sensitivity to the rate at which the aortic valve transitioned between open and closed states. The late backward compression wave (3) is expected to depend strongly on the wave transmission characteristics of the vascular network itself. In the current work, the vascular segments were parameterised based on a simplifying assumption of constant wave speed that is likely to have led to reduced reflections and suppressed backward propagation, that may explain the diminished magnitude of this wave in comparison to experimental findings. Further discussions on the dependence of each wave on the underlying cardiac events are available in [59]. The myocardial perfusion, estimated by the arterial inflow into the porous domain is shown in Fig. 3.8. It can be seen that the model reproduces the layer-dependent perfusion pattern, including systolic subendocardial flow reversal and endo-to-epi redistribution of flow [97].



**Fig. 3.8.** (a) Vascular velocity and tissue pore pressures are shown for a late diastolic phase; (b) Myocardial perfusion throughout the cardiac cycle shows endo-to-epi fluid shift in systole. Perfusion was calculated as the sum of arterial outflow into the segments of the porous domain

In the following section, we present an extension of the current framework to enable a consistent comparison between the perfusion fields calculated by the current approach, with those which are clinically measured using non-invasive imaging.

### 3.4.2 Perfusion Imaging and Modelling

Perfusion MRI is employed in the assessment of tissue perfusion and provides information about the state of the coronary circulation over various vessel diameter scales. In contrast-enhanced perfusion MRI a bolus of gadolinium-based contrast agent (c.a.) is injected and a fast MRI acquisition is employed in order to obtain image information over every heart beat during the first pass of c.a. through the myocardium. An MR signal increase caused by the inflow of c.a. into the myocardial tissue is compromised in the region of perfusion defect. This can be qualitatively evaluated directly from the image data as shown in Fig. 3.9. A semiquantitative assessment of the time evolution of MR contrast in Fig. 3.10 demonstrates a delayed signal increase, lower peak signal and upslope in the diseased myocardium.

#### 3.4.2.1 Perfusion MRI Background

The particular behaviour of perfusion MRI depends on the pharmacokinetics of the c.a., for example extravascular agents diffuse freely through capillary membranes into extracellular space, whereas intravascular contrast agents bind strongly to plasma proteins and remain within the blood. There also exist c.a. that contain both extracellular and intravascular components. The c.a. concentration, bolus injection duration, and total quantity of c.a. that is administered will also affect the final perfusion images.

Combining rest and stress perfusion scans allows for a detailed functional evaluation. The high spatio-temporal resolution of perfusion MRI makes it possible to observe a number of typical physiological phenomena in *in vivo* conditions, for instance different perfusion levels in subendocardial and subepicardial zones [39] or

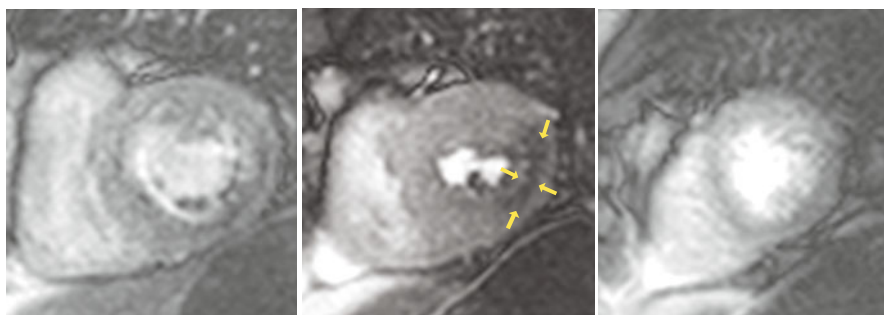


**Fig. 3.9.** Three slices of 2D perfusion MRI (covering base, mid-third and apical part of heart). Note the dark region in the mid-third of the lateral wall of left ventricle corresponding to the perfusion defect (yellow arrows). Courtesy of Prof. Eike Nagel, King's College London

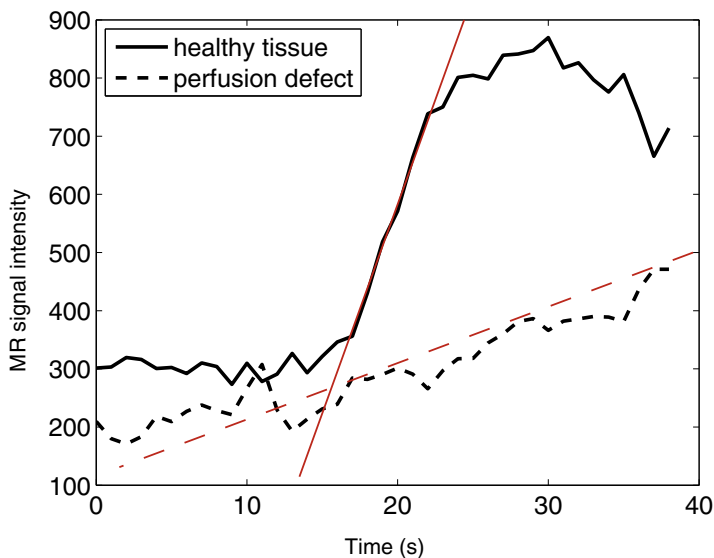


**Fig. 3.10.** Time evolution of MR signal in the middle slice of Fig. 3.9 with regions of interest placed into the healthy LV myocardium and into the perfusion defect. Note the lower peak signal and decreased upslope (dashed red line) in the hypoperfused region

the effect of phasic flow in the coronary circulation during cardiac cycle [81]. This demonstrates the significant potential of MRI in basic research – to better understand cardiac physiology both in healthy and diseased states – and in clinical research – to better stratify patients. Furthermore, the optimal adjustment of the many degrees of freedom in an MRI perfusion exam – some of which have been mentioned above – could ultimately also enhance the diagnostic efficacy of perfusion MRI.

### 3.4.2.2 Contrast Agent Transport Modelling

Although contrast-enhanced perfusion MRI shows great promise, it currently remains a technique which is confined mainly to research environments. The determination of optimal imaging strategies is complicated by the vast array of scanning parameters that can be chosen, the multiple pathologies that the modality can reveal, competing spatial-temporal requirements, and the selection of appropriate contrast agents. In this context computational modelling provides a means to more efficiently assess new imaging protocols and accommodate these disparate requirements.

#### *Mathematical Description*

The suitability of porous media formulations for modelling myocardial perfusion was summarised in Sect. 3.3.3. These justifications remain valid for modelling perfusion imaging. However an additional consideration is that the imaging data against

which the model would be validated is already the result of a volume averaging process as a typical voxel in MR perfusion imaging has dimensions of approximately  $1.2 \times 1.2 \times 10$  mm (Fig. 3.9).

To model the transport of contrast agent through the coronary circulation requires, in the most basic form, two equations, which for the sake of brevity and ease of analysis are presented here in nondimensional form (for full derivation see [20] and earlier works [7] and [88]). The first, an advection-diffusion equation, tracks the transport of c.a. concentration (henceforth denoted  $c$ ) in the fluid phase of the porous medium, which represents the blood (denoted by superscript  $f$ ):

$$\frac{\partial c^f}{\partial t} + \mathbf{u} \cdot \nabla c^f = \frac{1}{Pe} \nabla^2 c^f - Da(1 - \phi^f)(c^f - c^s) + \frac{q}{\phi^f}. \quad (3.53a)$$

Note that  $\mathbf{u}$  is related to the Darcy velocity (Eq. 3.12a) as:  $w/\phi^f$ .

To track the transport of c.a. in the solid phase of the porous medium – representing the extravascular space of the myocardium (superscript  $s$ ) – a diffusion equation is used:

$$\frac{\partial c^s}{\partial t} = \frac{D_r}{Pe} \nabla^2 c^s + Da\phi^f(c^f - c^s). \quad (3.53b)$$

In these equations the concentration  $c$  is defined per phase volume, and therefore the product  $\phi c$  gives the concentration per total volume.  $D^f$  and  $D^s$  are the diffusion coefficients of the contrast agent in the blood and extracellular space, respectively. Finally,  $q$  is a volumetric source term, typically applied at a few nodal points to represent the largest epicardial feeding vessels. In this model a temporal Gaussian inflow pattern is used to approximate the dispersion the bolus undergoes as it travels to and through the large coronary arteries.

These two transport equations are coupled by a reaction term which accounts for the diffusion of contrast agent through the vessel walls and into the extracellular space of the myocardial tissue. This model assumes that the flux through this vessel wall is proportional to the concentration difference that exists across it, which is commonly used in membrane models. The constant of proportionality  $\alpha$  is a phenomenological parameter that encapsulates both the permeability of the vessel wall to a particular contrast agent molecule, and the efficiency of the vascular geometry at allowing mass transfer across its surface and into the tissue.

The four nondimensional parameters are defined as follows.

1. Peclet number ( $Pe$ ) =  $\frac{Ud}{D^f}$ , characterises the relative time scales of advective and diffusive processes in the blood.
2. Damköhler number ( $Da$ ) =  $\frac{\alpha d}{U}$ , characterises the relative rates with which contrast agent passes through the vessel wall and is swept past it by the blood.
3. Diffusivity ratio ( $D_r$ ) =  $\frac{D^s}{D^f}$ , indicates the relative importance of diffusive processes in the intra- and extravascular spaces.
4. Fluid porosity ( $\phi^f$ ), the volume fraction of the porous medium occupied by the blood.



Once the concentration value in each phase has been determined, the total concentration in the bulk volume can be calculated by the following porosity weighted sum of the component concentrations.

$$c^{total} = \phi^f c^f + \phi^s c^s. \quad (3.54a)$$

Denoting the signal response as  $I$ , the observed myocardial signal  $I^{myo}$  is given by:

$$I^{myo} = I(\phi^f, \phi^s, c^f, c^s). \quad (3.55)$$

Data characterising typical nonlinear signal responses  $I(c)$  can be found in [49] and [42]. In the linear regime of  $I$ , before the signal begins to saturate,  $c^{total}$  is proportional to the signal.

In the Darcy flow model zero Neumann conditions are specified on all surfaces of the domain, used for the results in Figs. 3.11 to 3.14. The flow is driven by mass source models of the arteries and distributed sink terms that model the venous circulation [46]. Similarly, zero Neumann boundary conditions are applied in the transport model, with concentration sources specified at the same locations as the fluid mass sources, as used to generate the results in Fig. 3.14. The diffusion equation of the transport model is discretised using the Galerkin finite element method, whilst the advection-diffusion equation uses a Petrov-Galerkin method with streamline up-winding to improve numerical stability of the advection operator. The discrete forms of both equations are assembled into a monolithically-coupled linear system, such that both concentration values are solved simultaneously. The time stepping is performed by a backward-Euler scheme.

### 3.4.2.3 Results

#### *Time Series Data*

These time series data are taken from an idealised model of perfusion in the capillaries. A rectangular domain – discretised with linear Lagrange, quadrilateral elements – is used to represent the capillary bed, with uniform inflow and outflow boundary conditions in the Darcy model. A point source of concentration is situated near to the inflow and the c.a. swept downstream.

Figures 3.11a–11d show pointwise values of the c.a. concentration (fluid, tissue and total) taken at the centre of the domain, downstream of the point of contrast agent injection, for four values of  $Da$ . All of the figures show the arrival, dispersion and subsequent wash-out of the c.a. bolus. Fig. 3.11a is the concentration signal for a blood-pool (intravascular) c.a., the case  $Da = 0$  and thus all the signal originates in the fluid phase, preserving the Gaussian nature of the input bolus. As  $Da$  is increased to 0.1 in Fig. 3.11b, a small quantity of c.a. now diffuses into the tissue phase, creating a long tail in the total signal as the c.a. slowly diffuses back into the blood to be transported away downstream. At  $Da = 1.0$ , Fig. 3.11d, the storage in the tissue is significant, causing the peak concentration to be roughly halved, but these levels of signal now persist for much longer. Note that because the transport of c.a. through

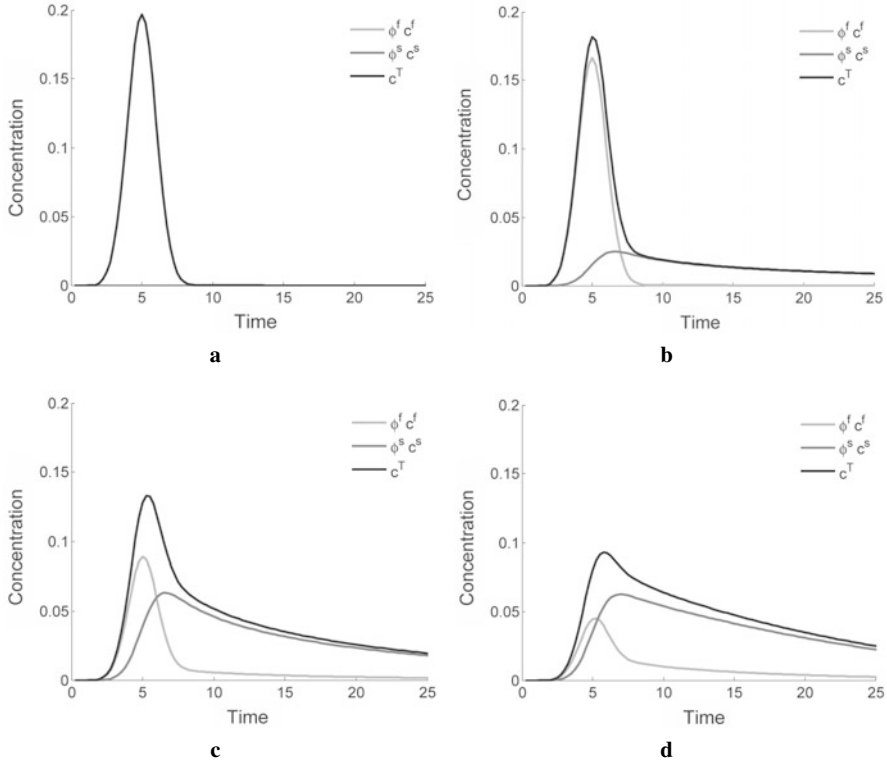


**Fig. 3.11.** Concentration time series data measured downstream from the c.a. injection point, for increasing values of  $Da$ . (a)  $Da = 0$ ; (b)  $Da = 0.1$ ; (c)  $Da = 0.5$ ; (d)  $Da = 1.0$ . Adapted from Cookson et al., 2014 [20]. Reproduced under the Creative Commons License 3.0 (<http://creativecommons.org/licenses/by/3.0/>)

the capillary walls is driven by the concentration difference between fluid and tissue, the c.a. enters the tissue much more quickly than it leaves.

### *Parameter Space Study*

A common method for quantitatively estimating perfusion proposed in the clinical literature uses the signal upslope [4] as a key part of the calculation. This upslope is defined as the maximum positive temporal gradient of the time series at a given point (see Fig. 3.10). It is therefore useful to understand the potential variation of this quantity with changing parameter values in the model, and thereby assess the impact on this quantification technique.

Figure 3.12 shows the variation of perfusion signal properties with changing  $Da$  and  $Dr$ . These plots reveal a previously-unknown non-monotonic behaviour in both the peak concentration and upslope with respect to changes in  $Da$ . Parameter estimation suggests that contrast agents currently used for cardiac perfusion imaging lie in

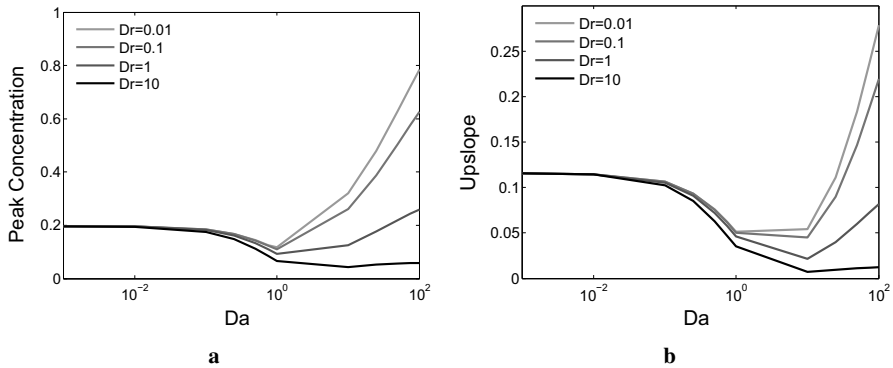


**Fig. 3.12.** Concentration signal properties display non-monotonic behaviour with respect to increases in  $Da$ , which means these properties alone are insufficient for use in parameter estimation. (a) Variation of peak concentration with  $Da$  and  $Dr$ ; (b) Variation of signal upslope with  $Da$  and  $Dr$ . Adapted from Cookson et al., 2014 [20]. Reproduced under the Creative Commons License 3.0 (<http://creativecommons.org/licenses/by/3.0/>)

the range of  $0.25 < Da < 2$ , indicating that this non-monotonic behaviour will be important for interpreting current perfusion images. Furthermore, within this estimated range, the signals are far more sensitive to changes in  $Da$  than they are in  $Dr$ .

Similar trends are observed when varying  $Pe$  and  $Da$ , while keeping the other parameters constant. As in Fig. 3.11, for fixed  $Pe$ , both signal properties display monotonic behaviour, with a minimum point at  $Da \approx 1$ . As  $Pe$  increases, both upslope and peak value increase, which is due to the reduced diffusion of the contrast agent bolus as it travels to the sampling point. Finally, both upslope and peak concentration are largely insensitive to the changes in porosity that might be expected to occur due to regional variation or tissue contraction during the cardiac cycle.

### *Simulating Perfusion Images*

Figure 3.13 shows the complete modelling framework with respect to its ability to represent a regional perfusion defect in the Darcy flow model, where the regional defect is defined based on the local vascular network in that area. This flow defect is then subsequently observable as an area of very low c.a. concentration in the transport model results. This 3D time-varying dataset can also be presented in the manner observed in clinical perfusion imaging, as in Fig. 3.14. This figure shows a set of three simulated imaging slices, with their locations along the heart long-axis marked. Clearly visible in the upper left portion of the slices is an area of dark blue, signifying low concentration of c.a. and therefore indicating a regional perfusion deficit.

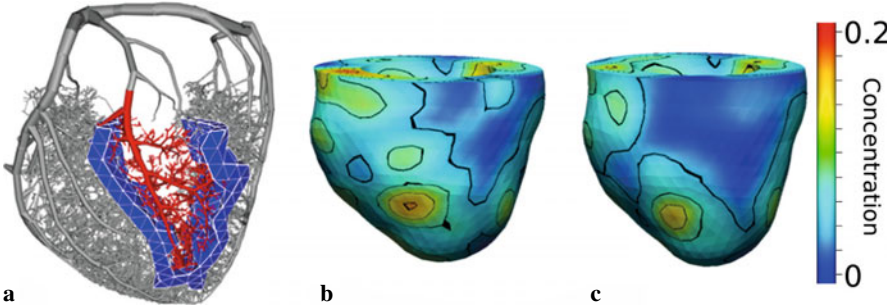


**Fig. 3.13.** (a) The cross-sectional area of the feeding artery of the red subtree was decreased by a factor of 0.7 to model stenosis of a branch of the coronary artery. Total concentration of contrast agent in the tissue 20 seconds after administering a bolus injection for a physiological case is shown in (b) and for the simulated occlusion of a coronary artery branch in (c). Adapted from Nolte et al. (2013) [72]

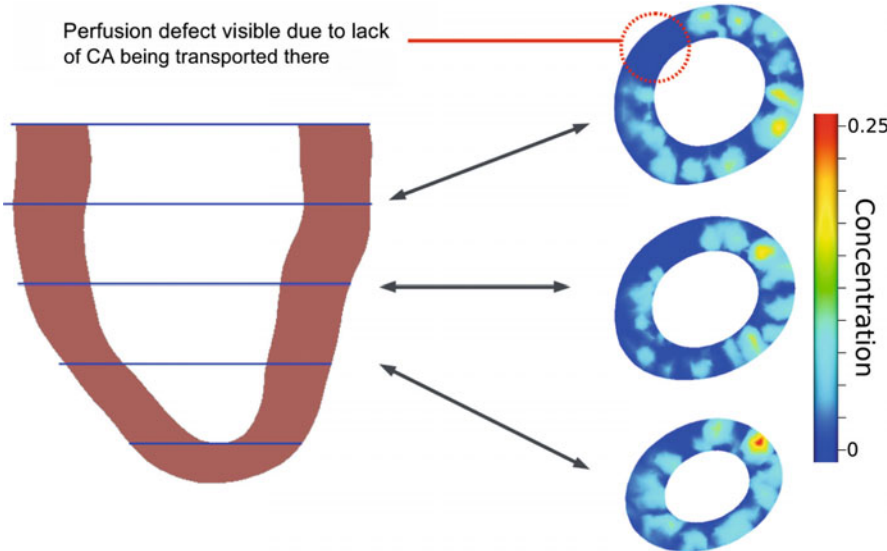


**Fig. 3.14.** A set of simulated perfusion images, taken at the three slice planes used in clinical imaging and using the non-dimensional form of the transport model. A perfusion defect is visible in the upper-left portion of the slices

### 3.5 Conclusions

In this chapter, we have presented a computational modelling framework coupling fluid and structure in order to simulate myocardial perfusion in a physiologically relevant manner. To this end we introduced a model of flow in macroscopic arteries, a multi-compartment Darcy model representing myocardial perfusion over

a range of vessel sizes and a poro-elastic model capturing the flow phenomena in the beating heart. The *in silico* obtained quantities – wave intensity and tissue signal in perfusion MRI, both of which represent the current state-of-the-art in invasive and non-invasive cardiological exams – create a basis for clinical translation of our work.

A key strength of wave intensity analysis in the coronary circulation is its ability to gauge the combined haemodynamic and mechanical function within a specific vascular territory and its associated myocardial region. Under the interventional clinical settings in which an acute coronary event must be managed with speed, WIA offers the potential to simplify the diagnostic procedure and improve its accuracy as recently demonstrated [26]. Despite these promises WIA is rarely, if at all, used in the current clinical landscape, one of the key reasons being that our understanding of the individual waves and their mechanistic origins is incomplete.

To this end we have approached the modelling of WIA via two complementary strategies representing the extremes of the clinical–physiological spectrum. The 1D model of the epicardial flow is oriented towards the real-time clinical usage, due to its reduced complexity, computational time and the amount data required to tune it. It aims to integrate the available *in vivo* patient data (simultaneous measurements of pressure and flow, and optionally the epicardial geometry and left ventricular pressure, if available) against the observed wave intensity characteristics to assess the impact of the disease on the distal and vessel mechanical parameters.

On the other hand, the poroelastic model provides a comprehensive framework with which to investigate the complex interaction between the aortic pressure, wave propagation and the myocardial contraction that underpins the change in the observed wave intensities. This approach facilitates investigations currently inaccessible to experimental means, due to the overwhelming complexity of acquiring such detailed measurements in the beating heart. Together with the 1D model, the combined approaches provide a tool for examination and interpretation of the clinically accessible invasive wave measurements.

In the perfusion MRI simulations we demonstrated the feasibility of coupling the porous medium flow model with advection-reaction-diffusion equations. In terms of validation and translation aspects, this capability to simulate the tracer-kinetic process underlying image formation is crucial to advancing the model into the realm of real-world relevance. The application of this work is primarily aimed at supporting the development of an optimal clinical non-invasive image acquisition protocol. Currently in perfusion MR imaging there are several open questions regarding the 2D vs 3D readout [50], spatio-temporal sampling resolution tradeoffs and the timing of data collection within the cardiac cycle [81]. While such investigations are generally tackled through direct population imaging studies, our integrated modelling framework has the capacity to contribute clarifications to these questions based on fundamental biophysical mechanisms. Further, the framework can be used to perform a parameter space exploration for the optimal design of imaging contrast agents, which is a costly and time-consuming exercise to undertake in the laboratory.

The added value of modelling in clinical practice lies in merging all patient information – beyond the qualitative intuition of the physician – and applying this integrated knowledge in the diagnosis and therapy planning. In this respect the next major challenge remaining in our clinical translation is the characterisation of the patient-specific parameters from clinical data. Of the various inverse estimation techniques available, the variational and sequential data assimilation approaches [16] have received particular recent interest in the cardiac community for image-based tuning of finite element models. To date, estimations of e.g. active [15, 48], passive [108, 109], electrical activation [22], myocardial fiber direction [70], vascular wall stiffness [9, 10] and aortic boundary tissue support parameters [66] have been reported. The application of such techniques to the models outlined in this chapter will reveal distal vascular parameters and porous permeability in a patient-specific manner. In concert with parallel efforts in the image analysis community on perfusion quantification [111] and associated emerging indices such as MRI gradient-togram [39], the modelling framework will enable a comprehensive assessment of regional perfusion in ischaemic heart disease.

With an expanded scope for real-world applications, the critical urgency of model validation must be emphasised. Whereas an experimental validation aims to ensure the model accurately reproduces the targeted physical and physiological phenomena, clinical validation is equally important for ensuring that the model will perform robustly on larger patient cohorts in spite of statistical and practical variations. In cardiovascular modelling, although a number of experimental validations have been performed to date [9, 11, 69, 93], clinical validation of models is at present infrequently attempted.

A notable recent exemplar for translation has been achieved through an application of 3D CFD to predict FFR from CT angiography data ( $\text{FFR}_{\text{CT}}$ ), bypassing the need for invasive procedures. This analysis, available as a commercial service, has undergone three prospective multicentre trials to date and has begun to be received by the medical community as a disruptive technology with the potential to transform clinical practice [28]. The outcomes of the most recent trial indicate that  $\text{FFR}_{\text{CT}}$  is capable of providing comparable sensitivity ( $\text{FFR}_{\text{CT}}$  86% vs CTA 94%) and a marked increase in specificity ( $\text{FFR}_{\text{CT}}$  79% vs CTA 34%), as compared to using CTA alone [73].

A key strength of the  $\text{FFR}_{\text{CT}}$  approach therefore derives from its capacity to extrapolate physiological function from purely anatomical information through modelling. But on the other hand, such a task inevitably involves assumptions regarding model parameters, necessitating their estimation from typical group behaviour. Therefore it is likely that the current gap between the diagnostic accuracy of  $\text{FFR}_{\text{CT}}$  and the gold standard invasive FFR is engendered by the intrinsic physiological variability among the individual patients. Particularly with regards to the distal circulation, a recent meta-analysis of published CFVR-FFR measurements showed that on the whole the therapeutic action recommended by these two indices disagree around 40% of the time, reflecting a potentially serious consequence of neglecting the relative contributions of focal, diffuse and microvascular disease in a specific individual [51]. Replacing the generic assumptions on maximal vasodilation of the distal

bed, minimal resistance level and flow distribution parameters with individualised estimations could help to bridge this gap.

At present the experimental validation of our modelling framework is under way, utilising previously established platforms of perfusion phantoms [19] and animal models [84]. Furthermore, recent advances in coronary MR imaging [63] open the future prospect for high-resolution MR-based anatomical characterisation of stenosis geometry that can leverage the perfusion imaging considered in this work. While the clinical utility of the framework remains to be elucidated through future trials, our experience so far has reinforced our belief that a fundamentally interdisciplinary approach is essential in developing new and effective strategies of disease management. A sufficient understanding of the problem through collaboration across multiple disciplines, holds the key to generating a truly revolutionary approach for understanding and treating coronary disease.

**Acknowledgements** The authors acknowledge funding from the Engineering and Physical Sciences Research Council (EP/G0075727/2, EP/J013250/1, EP/H046410/1), the Centre of Excellence in Medical Engineering funded by the Wellcome Trust and EPSRC (WT 088641/Z/09/Z) and British Heart Foundation Centre of Research Excellence hosted at King's College London (BHF RE/08/003). This research was supported by the National Institute for Health Research (NIHR) Biomedical Research Centre at Guy's and St Thomas' NHS Foundation Trust and King's College London. The views expressed are those of the author(s) and not necessarily those of the NHS, the NIHR or the Department of Health.

## References

1. Aguado-Sierra, J., Parker, K., Davies, J., Francis, D., Hughes, A., Mayer, J.: Arterial pulse wave velocity in coronary arteries. EMBS Annual International Conference, pp. 867–870 (2006)
2. Ambrosi, D., Quarteroni, A., Rozza, G.: Modeling of Physiological Flows, Springer, Milan (2012)
3. Anrep, G.V., Saalfeld, E.V.: The effect of the cardiac contraction upon the coronary flow. *J. Physiol.* **79**(3), 31–331 (1933)
4. Aquaro, G.D., Todiere, G., Di Bella, G., Guiducci, L., Pingitore, A., Lionetti, V.: A fast and effective method of quantifying myocardial perfusion by magnetic resonance imaging. *Int. J. Cardiovasc. Imaging.* **29**(6), 1313–1324 (2013)
5. Barnard, A., Hunt, W., Timlake, W., Varley, E.: A theory of fluid flow in compliant tubes. *Biophysical Journal* **6**(6) (1966)
6. J. Bear. Dynamics of Fluids in Porous Media. Number 2. Courier Dover Publications, (Aug. 1972)
7. Beaudoin, A., Dreuzy, J.-R., Erhel, J.: An efficient parallel particle tracker for advection-diffusion simulations in heterogeneous porous media, in: Kermarrec, A.-M., Bougé, L., Priol, T. (eds.): Euro-Par 2007 Parallel Processing, Lecture Notes in Computer Science 4641, pp. 717–726, Springer, Berlin Heidelberg (2007)
8. Beller, G.A., Zaret, B.L.: Contributions of nuclear cardiology to diagnosis and prognosis of patients with coronary artery disease, *Circulation* **101**, 1465–1478 (2000)

9. Bertoglio, C., Barber, D., Gaddum, N., Valverde, I., Rutten, M., Beerbaum, P., Moireau, P., Hose, R., Gerbeau, J.-F.: Identification of artery wall stiffness: in vitro validation and in vivo results of a data assimilation procedure applied to a 3D fluid-structure interaction model. *J. Biomech.* **47**(5), 1027–1034 (2014)
10. Bertoglio, C., Moireau, P., Gerbeau, J.-F.: Sequential parameter estimation in fluid-structure problems. Application to hemodynamics. *Int. J. Num. Meth. Biomed. Eng.* **28**, 434–455 (2012)
11. Bessems, D., Giannopapa, C.G., Rutten, M.C.M., van de Vosse, F.N.: Experimental validation of a time-domain-based wave propagation model of blood flow in viscoelastic vessels. *J. Biomech.* **41**(2), 284–291 (2008)
12. Bishop, A.H., Samady, H.: Fractional flow reserve: Critical review of an important physiologic adjunct to angiography, *American Heart Journal* **147**(5), 792–802 (2004)
13. Bruinsma, P., Arts, T., Dankelman, J., Spaan, J.: Model of the coronary circulation based on pressure dependence of coronary resistance and compliance. *Basic Research in Cardiology* **83**(5), 510–524 (1988)
14. Caruel, M., Chabiniok, R., Moireau, P., Lecarpentier, Y., Chapelle, D.: Dimensional reductions of a cardiac model for effective validation and calibration, *Biomechanics and Modeling in Mechanobiology* (2013), in press
15. Chabiniok, R., Moireau, P., Lesault, P.-F., Rahmouni, A., Deux, J.-F., Chapelle, D.: Estimation of tissue contractility from cardiac cine-MRI using a biomechanical heart model, *Biomechanics and modeling in mechanobiology* **11**(5), 609–30 (2012)
16. Chapelle, D., Fragu, M., Mallet, V., Moireau, P.: Fundamental principles of data assimilation underlying the Verdandi library: applications to biophysical model personalization within euHeart, *Medical & Biological Engineering & Computing* (2013)
17. Chapelle, D., Gerbeau, J.-F., Sainte-Marie, J., Vignon-Clementel, I.: A poroelastic model valid in large strains with applications to perfusion in cardiac modeling, *Computational Mechanics* **46**(1), 91–101 (2010)
18. Chilian, W.M., Layne, S.M., Klausner, E.C., Eastham, C.L., Marcus, M.L.: Redistribution of coronary microvascular resistance produced by dipyridamole. *American Journal of Physiology – Heart and Circulatory Physiology* **256**, H383–H390 (1989)
19. Chiribiri, A., Schuster, A., Ishida, M., Hautvast, G., Zarinabad, N., Morton, G., Otton, J., Plein, S., Breeuwer, M., Batchelor, P., Schaeffter, T., Nagel, E.: Perfusion phantom: An efficient and reproducible method to simulate myocardial first-pass perfusion measurements with cardiovascular magnetic resonance, *Magnetic Resonance in Medicine* **69**(3), 698–707 (2013)
20. Cookson, A.N., Lee, J., Michler, C., Chabiniok, R., Hyde, E., Nordsletten, D., Smith, N.P.: A spatially-distributed computational model to quantify behaviour of contrast agents in MR perfusion imaging. *Medical Image Analysis*, (in review) (2013)
21. Cookson, A.N., Lee, J., Michler, C., Chabiniok, R., Hyde, E.R., Nordsletten, D.A., Sinclair, M., Siebes, M., Smith, N.P.: A novel porous mechanical framework for modelling the interaction between coronary perfusion and myocardial mechanics, *J. Biomech.* **45**(5), 850–855 (2012)
22. Corrado, C., Gerbeau, J., Moireau, P.: Identification of weakly coupled multiphysics problems. Application to the inverse problem of electrocardiology, *J. Computational Physics* (in review) (2014)
23. Coussy, O.: *Mechanics of porous continua*. Wiley (1995)
24. Coussy, O.: *Poromechanics*. Wiley (2004)



25. Davies, J.E., Whinnett, Z.I., Francis, D.P., Manisty, C.H., Aguado-Sierra, J., Willson, K., Foale, R., Malik, I.S., Hughes, A.D., Parker, K.H., Mayet, J.: Evidence of a dominant backward-propagating "suction" wave responsible for diastolic coronary filling in humans, attenuated in left ventricular hypertrophy, *Circulation*, **113**(14), 1768–78 (2006)
26. De Silva, K., Foster, P., Guilcher, A., Bandara, A., Jogiyi, R., Lockie, T., Chowienyczk, P., Nagel, E., Marber, M., Redwood, S., Plein, S., Perera, D.: Coronary Wave Energy: A Novel Predictor of Functional Recovery After Myocardial Infarction, *Circulation. Cardiovascular interventions* (March 2013)
27. Dormieux, L., Kondo, D., Ulm, F.-J.: *Microporomechanics*, Wiley (2004)
28. Escaned, J.: Imaging: Can FFR<sub>CT</sub> replace old indices of coronary stenosis severity? *Nature Reviews Cardiology* (2014)
29. Factor, S.M., Okun, E.M., Minase, T., Kirk, E.S.: The microcirculation of the human heart: end-capillary loops with discrete perfusion fields, *Circulation*, **66**(6), 1241–1248 (1982)
30. Federico, S., Grillo, A.: Elasticity and permeability of porous fibre-reinforced materials under large deformations, *Mechanics of Materials* **44**, 58–71 (2012)
31. Fischer, J.J., Samady, H., McPherson, J.A., Sarembock, I.J., Powers, E.R., Gimple, L.W., Ragosta, M.: Comparison between visual assessment and quantitative angiography versus fractional flow reserve for native coronary narrowings of moderate severity, *The American Journal of Cardiology* **90**, 210–215 (2002)
32. Fiss, D.M.: Normal coronary anatomy and anatomic variations, *Supplement to Applied Radiology*, pp. 14–26 (2007)
33. Formaggia, L., Lamponi, D., Quarteroni, A.: One-dimensional models for blood flow in arteries, *Journal of Engineering Mathematics* (2002)
34. Formaggia, L., Nobile, F., Quarteroni, A., Veneziani, A.: Multiscale modelling of the circulatory system: a preliminary analysis, *Computing and visualization in science* **2**(2–3), 75–83 (1999)
35. Formaggia, L., Quarteroni, A., Veneziani, A.: *Cardiovascular Mathematics: Modeling and simulation of the circulatory system*, Springer, Milan (2009)
36. Fulton, W.F.M.: Arterial anastomoses in the coronary circulation. i. anatomical features in normal and diseased hearts demonstrated by stereoarteriography, *Scottish Med. J.* **8**, 420–434 (1963)
37. Gould, K.L., Kirkeeide, R.L., Buchi, M.: Coronary flow reserve as a physiologic measure of stenosis severity, *JACC* **15**(2), 459–474 (1990)
38. Gregg, D.E., Green, H.D.: Registration and interpretation of normal phasic inflow into the left coronary artery by an improved differential manometric method, *Am. J. Physiol.* **130**, 114–125 (1940)
39. Hautvast, G.L.T.F., Chiribiri, A., Lockie, T., Breeuwer, M., Nagel, E., Plein, S.: Quantitative analysis of transmural gradients in myocardial perfusion magnetic resonance images. *Magnetic Resonance in Medicine* **66**, 1477–1487 (2011)
40. Helfant, R.H., Vokonas, P.S., Gorlin, R.: Functional importance of the human coronary collateral circulation, *New England Journal of Medicine* **284**(23), 1277–1281 (1971)
41. Holzapfel, G.A., Ogden, R.W.: Constitutive modelling of passive myocardium: a structurally based framework for material characterization, *Philosophical transactions. Series A, Mathematical, physical, and engineering sciences* **367**(1902), 3445–75 (2009)
42. Hsu, L.-Y., Kellman, P., Arai, A.E.: Nonlinear myocardial signal intensity correction improves quantification of contrast-enhanced first-pass MR perfusion in humans, *J. Magn. Reson. Imaging* **27**(4), 793–801 (2008)

43. Hughes, T.J., Lubliner, J.: On the one-dimensional theory of blood flow in the larger vessels (1973)
44. Huyghe, J.M., Arts, T., van Campen, D.H., Reneman, R.S.: Porous medium finite element model of the beating left ventricle, *American Journal of Physiology-Heart and Circulatory Physiology* **262**(4), H1256–H1267 (1992)
45. Huyghe, J.M., Van Campen, D.H.: Finite deformation theory of hierarchically arranged porous solids. I: Balance of mass and momentum, *International J. Engineering Science* **33**(13), 1861–1871 (1995)
46. Hyde, E.R., Cookson, A.N., Lee, J., Michler, C., Goyal, A., Sochi, T., Chabiniok, R., Sinclair, M., Nordsletten, D.A., Spaan, J., van den Wijngaard, J.P.H.M., Siebes, M., Smith, N.P.: Multi-Scale Parameterisation of a Myocardial Perfusion Model Using Whole-Organ Arterial Networks, *Annals of biomedical engineering* (Dec. 2013)
47. Hyde, E.R., Michler, C., Lee, J., Cookson, A.N., Chabiniok, R., Nordsletten, D.A., Smith, N.P.: Parameterisation of multi-scale continuum perfusion models from discrete vascular networks, *Med. Biol. Eng. Comput.* **51**(5), 557–570 (2013)
48. Imperiale, A., Chabiniok, R., Moireau, P., Chapelle, D.: Constitutive Parameter Estimation Using Tagged-MRI Data. In D.N. Metaxas and L. Axel, editors, *FIMH'11 – Sixth International Conference on Functional Imaging and Modeling of the Heart*, vol. 6666, pp. 409–417, Springer, New York (2011)
49. Ishida, M., Sakuma, H., Murashima, S., Nishida, J., Senga, M., Kobayasi, S., Takeda, K., Kato, N.: Absolute blood contrast concentration and blood signal saturation on myocardial perfusion MRI: Estimation from CT data, *J. Magnetic Resonance Imaging* **29**(1), 205–210 (2009)
50. Jogiya, R., Kozerke, S., Morton, G., De Silva, K., Redwood, S., Perera, D., Nagel, E., Plein, S.: Validation of dynamic 3-dimensional whole heart magnetic resonance myocardial perfusion imaging against fractional flow reserve for the detection of significant coronary artery disease, *JACC* **60**(5), 756–765 (2012)
51. Johnson, N.P., Kirkeeide, R.L., Gould, K.L.: Is discordance of coronary flow reserve and fractional flow reserve due to methodology or clinically relevant coronary pathophysiology? *JACC Cardiovasc Imaging* **5**(2), 193–202 (2012)
52. Judd, R.M., Levy, B.I.: Effects of barium-induced cardiac contraction on large- and small-vessel intramyocardial blood volume, *Circulation Research* **56**(3), 293–309 (1985)
53. Kajiya, F., Tomonaga, G., Tsujioka, K., Ogasawara, Y., Nishihara, H.: Evaluation of local blood flow velocity in proximal and distal coronary arteries by laser Doppler method, *Journal of biomechanical engineering* **107**, 10–15 (1985)
54. Kassab, G.S.: Scaling laws of vascular trees: of form and function, *Am J Physiol.*, (2006) 290:H894–903
55. Kassab, G.S., Rider, C.A., Tang, N.J., Fung, Y.: Morphometry of pig coronary arterial trees. *Am. J. Physiol.* **265**, 350–365 (1993)
56. Kerckhoffs, R., Bovendeerd, P., Prinzen, F., Smits, K., Arts, T.: Intra-and interventricular asynchrony of electromechanics in the ventricularly paced heart, *J. Engineering Mathematics* **47**(3–4), 201–216 (2003)
57. Kim, H.J., Vignon-Clementel, I.E., Coogan, J.S., Figueroa, C.A., Jansen, K.E., Taylor, C.A.: Patient-specific modeling of blood flow and pressure in human coronary arteries, *Annals of Biomedical Engineering* **38**(10), 3195–209 (2010)
58. Lee, J., Cookson, A., Roy, I., Kerfoot, E., Asner, L., Viguera, G., Sochi, T.: C. Michler, N. Smith, and D. Nordsletten. Cheart: A multi-physics parallel computing engine, in prep.

59. Lee, J., Nordsletten, D., Cookson, A., Rivolo, S., Smith, N.: In silico coronary wave intensity analysis: cardiac function to wave generating mechanisms, *J. Physiology*, in review
60. Lee, J., Smith, N.: Development and application of a one-dimensional blood flow model for microvascular networks. *Proceedings of the Institution of Mechanical Engineers, Part H, J. Engineering in Medicine* **222**, 487–511 (2008)
61. Lee, J., Smith, N.P.: The Multi-Scale Modelling of Coronary Blood Flow, *Annals of biomedical engineering* (May 2012)
62. Zamir, H.C.M.: Branching characteristics of human coronary arteries, *Can. J. Physiol. Pharmacol.* **64**, 661–668 (1986)
63. Makowski, M.R., Henningsson, M., Spuentrup, E., Kim, W.Y., Maintz, D., Manning, W., Botnar, R.: Characterization of coronary atherosclerosis by magnetic resonance imaging, *Circulation* **128**, 1244–1255 (2013)
64. Matthys, K.S., Alastruey, J., Peiró, J., Khir, A.W., Segers, P., Verdonck, P.R., Parker, K.H., Sherwin, S.J.: Pulse wave propagation in a model human arterial network: assessment of 1-D numerical simulations against in vitro measurements, *J. biomechanics* **40**(15), 3476–86 (2007)
65. Meier, P., Gloekler, S., Zbinden, R., Beckh, S., de Marchi, S.F., Zbinden, S., Wustmann, K., Billinger, M., Vogel, R., Cook, S., Wenaweser, P., Togni, M., Windecker, S., Meier, B., Seiler, C.: Beneficial effect of recruitable collaterals a 10-year follow-up study in patients with stable coronary artery disease undergoing quantitative collateral measurements, *Circulation* **116**(9), 975–983 (2007)
66. Moireau, P., Bertoglio, C., Xiao, N., Figueroa, C.A., Taylor, C., Chapelle, D., Gerbeau, J.-F.: Sequential identification of boundary support parameters in a fluid-structure vascular model using patient image data, *Biomechanics and Modeling in Mechanobiology* **12**(3), 475–496 (2012)
67. Murray, S.W., Rathore, S., Stables, R.H., Palmer, N.D.: Contemporary coronary imaging from patient to plaque – part 1: IVUS-derived virtual histology, *British J. Cardiology* **17**(3), 129–132 (2010)
68. Mynard, J.P., Nithiarasu, P.: A 1D arterial blood flow model incorporating ventricular pressure, aortic valve and regional coronary flow using the locally conservative Galerkin (LCG) method, *Communications In Numerical Methods In Engineering*, 367–417 (March 2008)
69. Mynard, J.P., Penny, D.J., Smolich, J.J.: Scalability and in-vivo validation of a multi-scale numerical model of the left coronary circulation, *American J. Physiology – Heart and Circulatory Physiology* (2013)
70. Nagler, A., Bertoglio, C., Gee, M., Wall, W.: Personalization of cardiac fiber orientations from image data using the unscented kalman filter. In S. Ourselin, D. Rueckert, and N. Smith, editors, 7th International Conference on Functional Imaging and Modeling of the Heart, FIMH 2013, Lecture Notes in Computer Science 7945, pp. 132–140. Springer-Verlag, Berlin Heidelberg (2013)
71. Niederer, S.A., Plank, G., Chinchapatnam, P., Ginks, M., Lamata, P., Rhode, K.S., Rinaldi, C.A., Razavi, R., Smith, N.P.: Length-dependent tension in the failing heart and the efficacy of cardiac resynchronization therapy, *Cardiovascular Research* **89**(2), 336–343 (2011)

72. Nolte, F., Hyde, E.R., Rolandi, C., Lee, J., van Horssen, P., Asrress, K., van den Wijngaard, J.P.H.M., Cookson, A.N., van de Hoef, T., Chabiniok, R., Razavi, R., Michler, C., Hautvast, G.L.T.F., Piek, J.J., Breeuwer, M., Siebes, M., Nagel, E., Smith, N.P., Spaan, J.A.E.: Myocardial perfusion distribution and coronary arterial pressure and flow signals: clinical relevance in relation to multiscale modeling, a review, *Med. Biol. Eng. Comput.* **51**(11), 1271–1286 (2013)
73. Nørgaard, B.L., Leipsic, J., Gaur, S., Seneviratne, S., Ko, B.S., Ito, H., Jensen, J.M., Mauri, L., De Bruyne, B., Bezerra, H., et al.: Diagnostic performance of non-invasive fractional flow reserve derived from coronary ct angiography in suspected coronary artery disease: The NXT trial, *J. American College of Cardiology* (2014)
74. Obaid, D.R., Murray, S.W., Palmer, N.D., Rudd, J.H.F.: Contemporary coronary imaging from patient to plaque – part 3: cardiac computed tomography, *British J. Cardiology* **17**(5), 235–239 (2010)
75. Olufsen, M.: Structured tree outflow condition for blood flow in larger systemic arteries, *American J. Physiology – Heart and Circulatory Physiology* (1999)
76. Parker, K.H.: An introduction to wave intensity analysis, *Medical & biological engineering & computing* **47**(2), 175–88 (2009)
77. Pedley, T.J.: *The Fluid Mechanics of Large Blood Vessels* (1980)
78. Pijls, N.H., van Son, J.A., Kirkeeide, R.L., De Bruyne, Gould, K.L.: Experimental basis of determining maximum coronary, B., myocardial, and collateral blood flow by pressure measurements for assessing functional stenosis severity before and after percutaneous transluminal coronary angioplasty, *Circulation* **87**, 1354–1367 (1993)
79. Pindera, M.Z., Ding, H., Athavale, M.M., Chen, Z.: Accuracy of 1D microvascular flow models in the limit of low Reynolds numbers, *Microvascular research* **77**(3), 273–280 (2009)
80. Prinzen Bassingthwaighte, J.B.: Blood flow distributions by microsphere deposition methods, F.W., *Cardiovascular Research* **45**, 13–21 (2000)
81. Radjenovic, A., Biglands, J.D., Larghat, A., Ridgway, J.P., Ball, S.G., Greenwood, J.P., Jerosch-Herold, M., Plein, S.: Estimates of systolic and diastolic myocardial blood flow by dynamic contrast-enhanced MRI, *Magnetic Resonance in Medicine* **64**, 1696–1703 (2010)
82. Rathore, S., Murray, S., Stables, R., Palmer, N.: From patient to plaque. contemporary coronary imaging, part 2: optical coherence tomography, *British J. Cardiology* **17**(4), 190–193 (2010)
83. Reymond, P., Merenda, F., Perren, F., Rüfenacht, D., Stergiopulos, N.: Validation of a one-dimensional model of the systemic arterial tree, *American J. Physiology, Heart and circulatory physiology* **297**(1), H208–222 (2009)
84. Schuster, A., Grünwald, I., Chiribiri, A., Southworth, R., Ishida, M., Hay, G., Neumann, N., Morton, Perera, D., G., Schaeffter, T., Nagel, E.: An isolated perfused pig heart model for the development, validation and translation of novel cardiovascular magnetic resonance techniques, *J. Cardiovascular Magnetic Resonance* **12**(53) (2010)
85. Sherwin, S., Formaggia, L., Peiro, J.: Computational modelling of 1D blood flow with variable mechanical properties and its application to the simulation of wave propagation in the human arterial system, *International J. Numerical Methods in Fluids* **43**, 673–700 (2003)
86. Sherwin, S.J., Alastruey, J., Parker, K.H., Peir, J.: Lumped Parameter Outflow Models for 1-D Blood Flow Simulations: Effect on Pulse Waves and Parameter Estimation, *Communications in Computational Physics* **4**(2), 317–336 (2008)

87. Sherwin, S.J., Franke, V., Peir, J., Parker, K.H.: One-dimensional modelling of a vascular network in space-time variables, *J. Engineering Mathematics* **47**, 217–250 (2003)
88. R. Shipley and S. Chapman. Multiscale modelling of fluid and drug transport in vascular tumours, *Bulletin of Mathematical Biology* **72**(6), 1464–1491 (2010)
89. Smith, N.P., Pullan, A.J., Hunter, P.J.: An Anatomically Based Model of Transient Coronary Blood Flow in the Heart, *SIAM J. Applied Mathematics* **62**(3), 990 (2002)
90. Spaan, J.A.E.: Coronary diastolic pressure-flow relation and zero flow pressure explained on the basis of intramyocardial compliance, *Circulation Research* **56**(3), 293–309 (1985)
91. Spaan, J.A.E., Kolyva, C., van den Wijngaard, J.P.H.M., ter Wee, R., van Horssen, P., Piek, J.J., Siebes, M.: Coronary structure and perfusion in health and disease. *Philosophical transactions, Series A, Mathematical, physical, and engineering sciences* **366**(1878), 3137–53 (2008)
92. Spaan, J.A.E., Siebes, M., Wee, R., Kolyva, C., Vink, H., Fokkema, D.S., Streekstra, G., Vanbavel, E.: Visualisation of intramural coronary vasculature by an imaging cryomicrotome suggests compartmentalisation of myocardial perfusion areas, *Med. Biol. Eng. Comput.* **43**, 43–435 (2005)
93. Steele, B.N., Wan, J., Ku, J.P., Hughes, T.J.R., Taylor, C.A.: In vivo validation of a one-dimensional finite-element method for predicting blood flow in cardiovascular bypass grafts, *IEEE Trans. Biomed. Eng.* **50**(6), 649–656 (2003)
94. Stettler, J., Niederer, P., Anliker, M.: Theoretical analysis of arterial hemodynamics including the influence of bifurcations, *Annals of Biomedical Engineering* **9**(2), 145–164 (1981)
95. Taylor, C.A., Steinman, D.A.: Image-based modeling of blood flow and vessel wall dynamics: applications, methods and future directions, *Annals of Biomedical Engineering* **38**(3), 1188–1203 (2010)
96. Topol, J.E., Nissen, S.E.: Our preoccupation with coronary luminology, *Circulation* **92**, 2333–2342 (1995)
97. Toyota, E., Ogasawara, Y., Hiramatsu, O., Tachibana, H., Kajiya, F., Yamamori, S., Chilian, W.M.: Dynamics of flow velocities in endocardial and epicardial coronary arteries, *American Journal of Physiology-Heart and Circulatory Physiology* **57**(4), H1598 (2005)
98. Traupe, T., Gloekler, S., de Marchi, S.F., Werner, G.S., Seiler, C.: Assessment of the human coronary collateral circulation, *Circulation* **122**(12), 1210–1220 (2010)
99. van de Vosse, F.N., Stergiopulos, N.: Pulse Wave Propagation in the Arterial Tree, *Annual Review of Fluid Mechanics* **43**(1), 467–499 (2011)
100. van den Wijngaard, J.P.H.M., van Horssen, P., ter Wee, R., Coronel, R., de Bakker, J.M., de Jonge, N., Siebes, M., Spaan, J.A.E.: Organization and collateralization of a subendocardial plexus in end-stage human heart failure, *American J. Physiology – Heart and circulatory physiology* **298**(1), H158–62 (2010)
101. Vankan, W., Huyghe, J., Janssen, J.: Poroelasticity of saturated solids with an application to blood perfusion, *Int. J. Eng. Sci.* **34**(9), 1019–1031 (1996)
102. Vankan, W.J., Huyghe, J.M., Janssen, J.D., Huson, A., Schreiner, W.: Finite element blood flow through biological tissue, *Int. J. Engng. Sci.* **35**(4), 375–385 (1997)
103. Vignon, I., Taylor, C.: Outflow boundary conditions for one-dimensional finite element modeling of blood flow and pressure waves in arteries, *Wave Motion* **39**(4), 361–374 (2004)

104. Werner, G.S., Ferrari, M., Heinke, S., Kuethé, F., Surber, R., Richartz, B.M., Figulla, H.R.: Angiographic assessment of collateral connections in comparison with invasively determined collateral function in chronic coronary occlusions, *Circulation* **107**(15), 1972–1977 (2003)
105. Westerhof, N., Boer, C., Lamberts, R., Sipkema, P.: Cross-talk between cardiac muscle and coronary vasculature, *Physiol. Rev.* **86**, 1263–1308 (2006)
106. Westerhof, N., Lankhaar, J.-W., Westerhof, B.: The arterial windkessel, *Medical & Biological Engineering & Computing* **47**(2), 131–141 (2009)
107. Willemet, M., Lacroix, V., Marchandise, E.: Inlet boundary conditions for blood flow simulations in truncated arterial networks, *J. Biomechanics* **44**(5), 897–903 (2011)
108. Xi, J., Lamata, P., Lee, J., Moireau, P., Chapelle, D., Smith, N.: Myocardial transversely isotropic material parameter estimation from in-silico measurements based on reduced-order unscented Kalman filter, *J. mechanical behavior of biomedical materials* **4**(7), 1090–1102 (2011)
109. Xi, J., Lamata, P., Shi, W., Niederer, S., Land, S., Rueckert, D., Duckett, S.G., Shetty, A.K., Rinaldi, C.A., Razavi, R., Smith, N.: An Automatic Data Assimilation Framework for Patient-Specific Myocardial Mechanical Parameter Estimation, in: Metaxas, D.N., Axel, L. (eds.), *FIMH'11 – Sixth International Conference on Functional Imaging and Modeling of the Heart*, vol. 6666, pp. 392–400, Springer, New York (2011)
110. Zamir, M.: Cost analysis of arterial branching in the cardiovascular systems of man and animals, *J. Theor. Biol.* **120**, 111–23 (1986)
111. Zarinabad, N., Chiribiri, A., Breeuwer, M.: Myocardial blood flow quantification from MRI – an image analysis perspective, *Current Cardiovascular Imaging Reports* **7**(1), 1–9 (2014)